

# MUSE spectroscopy of the ULX NGC 1313 X-1: A shock-ionised bubble, an X-ray photoionised nebula, and two supernova remnants

A. Gúrpide<sup>1</sup>, M. Parra<sup>1,2</sup>, O. Godet<sup>1</sup>, T. Contini<sup>1</sup> and J.-F. Olive<sup>1</sup>

<sup>1</sup> IRAP, Université de Toulouse III/CNRS/CNES, 9 av. du Colonel Roche 31028 Toulouse, Cedex 04, France

<sup>2</sup> Univ. Grenoble Alpes, CNRS, IPAG, 38000 Grenoble, France

## ABSTRACT

**Context.** The presence of large ionised gaseous nebulae found around some ultraluminous X-ray sources (ULXs) provides the means to assess the mechanical and radiative feedback of the central source, and hence constrain the efficiency and impact on the surroundings of the super-Eddington regime powering most of these sources. NGC 1313 X-1 is an archetypal ULX, reported to be surrounded by abnormally high  $[\text{O I}]/\lambda 6300/\text{H}\alpha > 0.1$  ratios, and for which high-resolution spectroscopy in X-rays has hinted at the presence of powerful outflows.

**Aims.** We report observations taken with the integral field unit Multi-Unit Spectroscopic Explorer (MUSE) mounted at the Very Large Telescope of NGC 1313 X-1 in order to confirm the presence of a nebula inflated by the winds, investigate its main sources of ionisation and estimate the mechanical output of the source.

**Methods.** We investigated the morphology, kinematics, and sources of ionisation of the bubble through the study of the main nebular lines. We compared the main line ratios with spatially resolved Baldwin–Phillips–Terlevich diagrams and with the prediction from radiative shock libraries, which allows us to differentiate regions excited by shocks from those excited by extreme ultraviolet and X-ray radiation.

**Results.** We detect a bubble of  $452 \times 266$  pc in size, roughly centred around the ULX, which shows clear evidence of shock ionisation in the outer edges. We estimate shock velocities to be in the  $\approx 160 - 180$  km/s range based on the line ratios. This suggests that an average and continuous outflow power of  $\sim (2 - 4.5) \times 10^{40}$  erg/s over a timescale of  $(4.5 - 7.8) \times 10^5$  yr is required to inflate the bubble. In the interior of the bubble and closer to the ULX we detect an extended ( $\sim 140$  pc) X-ray ionised region. Additionally, we detect two supernova remnants coincidentally close to the ULX bubble of which we also report age and explosion energy estimates.

**Conclusions.** The elongated morphology and the kinematics of the bubble strongly suggest that the bubble is being inflated by winds and/or jets emanating from the central source, supporting the presence of winds found through X-ray spectroscopy. The estimated mechanical power is comparable to or higher than the X-ray luminosity of the source, which provides additional evidence in support of NGC 1313 X-1 harbouring a super-Eddington accretor.

**Key words.** X-rays: binaries – Accretion – Stars: neutron – Stars: black holes – ISM: bubbles – ISM: jets and outflows – instrumentation: spectrographs

## 1. Introduction

Ultraluminous X-ray sources (ULXs) are an enigmatic class of objects empirically defined as extragalactic, point-like, off-nuclear, and with an X-ray luminosity exceeding the classical Eddington limit for a  $\sim 20 M_{\odot}$  black hole (BH) (see Fabrika et al. 2021, for the most recent review). While this empirical definition alone does not convey much information about the nature of these objects, there is now firm evidence suggesting that a fraction of them are powered by super-Eddington accretion onto stellar-compact objects. Evidence in support of this picture comes from their atypical X-ray spectral states compared to sub-Eddington X-ray binaries (e.g. Gladstone et al. 2009; Bachetti et al. 2013; Gúrpide et al. 2021b), the discovery of X-ray pulsations in several ULXs with luminosities exceeding the classical Eddington limit for a neutron star (NS) by orders of magnitude (e.g. Bachetti et al. 2014; Fürst et al. 2016; Israel et al. 2017; Carpano et al. 2018; Sathyaprakash et al. 2019; Rodríguez-Castillo et al. 2020; Quintin et al. 2021), the detection of strongly Doppler shifted X-ray lines indicative of super-Eddington winds with speeds reaching fractions of the speed

of light (e.g. Pinto et al. 2016, 2020b, 2021), the inflated or photoionised 40–400 pc optical and radio bubbles found around them (Pakull & Mirioni 2002; Abolmasov et al. 2007; Berghea et al. 2020), and their similarities with the supercritically accreting Galactic source SS433 (Fabrika 2004; Liu et al. 2015; Waisberg et al. 2019; Middleton et al. 2021). While these observational clues appear to match our understanding of the super-Eddington accretion regime to some extent (e.g. Shakura & Sunyaev 1973; Poutanen et al. 2007; Takeuchi et al. 2013; Jiang et al. 2014; Middleton et al. 2015; Narayan et al. 2017), many questions about the super-Eddington regime and its connection with ULXs remain open, such as the degree to which the emission is beamed (e.g. King et al. 2001; Kaaret et al. 2004; Jiang et al. 2014; Mushtukov et al. 2021), the fraction of energy carried in the outflows, the mechanical and radiative feedback induced by ULXs, and the exact accretion flow geometry allowing them to reach such high luminosities.

Because the X-ray luminosity is the defining property of a ULX, it is natural that most studies attempting to tackle these issues have focused on the X-ray band (e.g. Middleton et al. 2015; Koliopanos et al. 2017; Walton et al. 2018; Gúrpide et al.

2021a). However, observations in this band are generally limited by our ability to obtain information restricted to our line of sight. For this reason, testing the degree of anisotropy of the X-ray emission remains challenging (e.g. Middleton et al. 2021), yet strong anisotropy is predicted in many theoretical studies of the super-Eddington accretion regime (e.g. Shakura & Sunyaev 1973; Poutanen et al. 2007; Narayan et al. 2017) and is a fundamental piece of information to determine the true radiative output in this poorly understood accretion regime.

On the other hand, the study of ULX bubbles offers the means to infer this energetic output by observing the impact of the ULX on the environment. Because the bubble nebula sees the full emission from the ULX, it essentially offers a 2D map of the ionising photon field emitted by the ULX, while also probing the presence and the impact of the super-Eddington winds or jets on the environment. Therefore, ULX nebulae can be used to constrain the energetics and overall properties of the super-Eddington accretion flows powering ULXs. A prime example is the study of the ULX nebula around the ULX NGC 6946 X-1 by Abolmasov et al. (2008), who showed that the presence of a UV source with  $L \sim 10^{40}$  erg/s was needed to explain the high-excitation lines of the nebula. Later *HST* observations in the far-UV by Kaaret et al. (2010) confirmed the presence of the first ultraluminous UV source, in good agreement with the predictions made by Abolmasov et al. (2008). Observations of the HeII $\lambda$ 4686 recombination line of the X-ray photoionised nebula around Holmberg II X-1 have also been used to constrain the intrinsic X-ray flux of the source, finding that the degree of beaming of the X-ray emission must be small (Pakull & Mirioni 2002; Kaaret et al. 2004; Berghea et al. 2010). ULX nebulae are also of interest because they allow us to probe faint X-ray sources with luminosities below the ULX threshold, but for which most of the X-ray radiation might be simply not directed into our line of sight, or for which most of the energy might be released mechanically (Dubner et al. 1998; Pakull et al. 2010; Urquhart et al. 2019).

With integral field unit (IFU) instruments, the study of ULX nebulae becomes even more attractive as all the information needed to diagnose the physical conditions of the gas can be accessed with a single exposure. Indeed, several promising results can already be found in the literature (e.g. Egorov et al. 2017; McLeod et al. 2019). For this reason, we are undertaking a programme to search for ULXs directly or serendipitously observed by the Multi-Unit Spectroscopic Explorer (MUSE, Bacon et al. 2017), an IFU instrument at the Very Large Telescope (VLT) covering the 480–930 nm range, with a resolving power of  $\sim 2484$  at 650 nm.

In this paper we report the first of these analyses focusing on the well-known ULX NGC 1313 X-1 (e.g. Feng & Kaaret 2006; Bachetti et al. 2013). NGC 1313 X-1 has a persistent unabsorbed luminosity in the 0.3–10 keV band above  $\sim 8 \times 10^{39}$  erg/s, with a mean luminosity of  $1.1 \times 10^{40}$  erg/s (Gúrpide et al. 2021a). It is among the few ULXs for which high-resolution spectroscopy has hinted the presence of powerful winds with velocities  $\approx 0.2c$  (Pinto et al. 2016, 2020b; see also Walton et al. 2016), suggesting that the source harbours a supercritically accreting source, but whose nature remains unclear (Walton et al. 2020). It has been argued that the source should be seen at low inclinations, through the optically thin funnel formed by the wind around the rotational axis of the compact object (e.g. Sutton et al. 2013; Middleton et al. 2015; Gúrpide et al. 2021a). While these winds are thought to be powerful enough to carve the aforementioned  $\sim 100$  pc bubbles sometimes seen around ULXs (Pinto et al. 2020a), to date this has not been directly confirmed. The

presence of a nebula around NGC 1313 X-1 was hinted at in the seminal study of Pakull & Mirioni (2002), who noted an exceptionally high [O I] $\lambda$ 6300/H $\alpha$   $> 0.1$  ratio surrounding the ULX. Here we report the detection and analysis of a well-defined elongated  $452 \times 266$  pc shock-ionised bubble, providing the first link between wind detections in X-rays and their large-scale impact on the surroundings. In the interior of the bubble we find line ratios typical of an X-ray photoionised nebula, consistent with the results from Pakull & Mirioni (2002).

Our focus here lies in investigating the main sources of ionisation of the bubble. Through different diagnostics and thanks to the MUSE data, we are able to spatially resolve and distinguish regions excited by shocks from those excited by extreme ultraviolet (EUV) and X-ray photoionisation from the ULX, providing important clues about the energy feedback of the source. We show that while the bubble is likely to have been inflated by a wind, the inner regions show clear evidence of hard photoionisation from the ULX.

Coincidentally, we detect two supernova remnants (SNRs) at the edge of the bubble, of which we also provide line ratios and estimates of their kinetic explosion energy. An illustrative comparison between the energy required to inflate the ULX bubble invoking a SNR and these bona fide SNRs is provided. We show that the explosion energy required to inflate the ULX bubble is orders of magnitude higher than that of the SNRs, strongly disavowing this hypothesis, in agreement with previous works.

NGC 1313 ( $z = 0.001568$ ) is a face-on SB(s)d spiral galaxy at a distance of 4.25 Mpc (Tully et al. 2016) with an inclination  $i = 48^\circ$  (Ryder et al. 1995). NGC 1313 X-1 is located in the northern part of the galaxy, within the inner  $46''$  ( $\sim 950$  pc) radius from the nucleus of NGC 1313, where Ryder et al. (1995) determined the rotational velocity to be 46.5 km/s. This gives a line-of-sight velocity at the source position of  $V_{\text{rot}} \sin i \cos \theta \sim 30$  km/s over the systemic velocity, where  $\theta$  is the azimuth angle in the disk plane as defined by (Ryder et al. 1995) and at the position of NGC 1313 X-1  $\theta = 30^\circ$ .

This paper is organised as follows. Section 2 presents the observations considered and the data reduction. Section 3 presents our analysis and results of the ULX bubble and the SNRs. In Section 4 we discuss our results and implications. Finally we present our conclusion in Section 5.

## 2. Data reduction

NGC 1313 X-1 has been observed by MUSE in the Wide Field Mode (WFM) in three instances (PI F.P.A. Vogt) of 1.4 ks exposure time each. Two of these observations were taken in extended mode, which extends the observable bandpass in the blue part of the spectrum down to  $\sim 465$  nm, compared to the nominal mode that reaches only to  $\sim 480$  nm. The data cubes were downloaded from the ESO Science Portal<sup>1</sup>, which provides the data reduced by the automatic dedicated pipeline (Weilbacher et al. 2020) and ready for scientific analysis.

After inspection of the cubes, we discarded cube ADP.2019-12-20T09 12 08.117 from the analysis as  $\sim 92\%$  of the spaxels had negative values, which rendered it unusable. We therefore considered only cubes ADP.2019-12-08T00:33:13.185 (cube 1) and ADP.2019-11-29T11:13:19.106 (cube 2) for the analysis (see Table 1 for details). We found that both cubes had around 5% of invalid pixels, which we interpolated using the  $3 \times 3 \times 3$  nearest pixels using the method available in the Zurich Atmosphere Purge (ZAP) tool (Soto et al. 2016).

<sup>1</sup> <http://archive.eso.org/scienceportal/home>

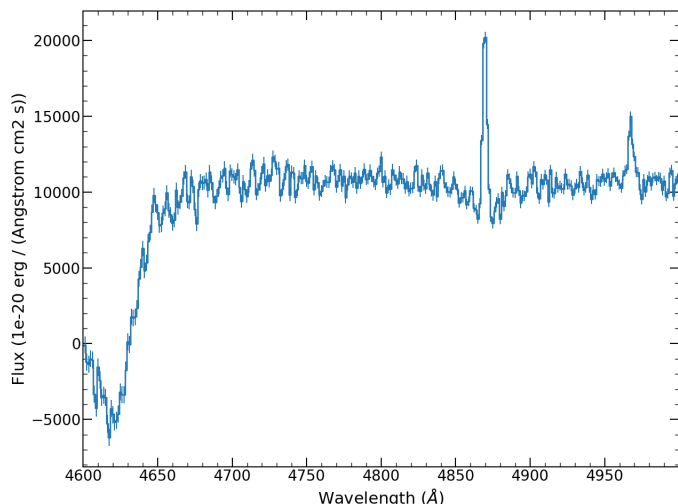


**Fig. 1.** Spectrum extracted from a pixel of cube ADP.2019-11-29T11:13:19.106 strongly affected by flux miscalibration effects at the blue edge of the wavelength range.

Cube 1 had slightly better spatial resolution (PSF FWHM  $\sim 1''$  vs  $1.2''$ ) and appeared of overall higher data quality as the sky subtraction had mostly affected the spectrum in the red part above  $\sim 7000 \text{ Å}$ , whereas in cube 2 the sky residuals are also observed around the  $\text{H}\alpha$ -[N II] complex. However, because the spatial distribution of the noise in each cube is different and the quality of each of the lines of interest depends strongly on the success of the sky correction, in some cases we could improve the results by combining the information from the two cubes (see Section 3.1). For this reason, we decided to analyse the two cubes independently and use them to cross-validate our results, although we mainly present the results from cube 1 for the reasons outlined above. We focused on the main nebular lines used for gas diagnostics covered by MUSE (i.e.  $\text{H}\beta$ , [O III] $\lambda 5007$ , [O I] $\lambda 6300$ , the  $\text{H}\alpha$ -[N II] complex, and the [S II] doublet). While cube 2 was taken in extended mode, in principle allowing us to measure  $\text{HeII}\lambda 4686$ , a relevant emission line in high-excitation nebulae (e.g. Kaaret et al. 2004), edge effects, and uncertainties on the flux calibration seemed to be affecting the cube in the blue part of the spectrum below  $4700 \text{ Å}$  (Figure 1), and thus we were unable to use this line in our analysis. The MUSE/WFM pixel scale of  $0.2''$  and the PSF FWHM of  $\sim 1''$  represent respectively a physical distance of  $4.2 \text{ pc}$  and  $\sim 20 \text{ pc}$  at the distance of NGC 1313 X-1 of  $4.25 \text{ Mpc}$ .

Along with the MUSE observations, we made use of archival *HST* data to correct the astrometry of the MUSE cubes and inspect the field around NGC 1313 X-1. In particular, we retrieved calibrated *HST* images from the Hubble Legacy Archive<sup>2</sup> in the ACS/WFC/F555W filter and in the WFC3/UVIS/F657N and WFC3/UVIS/547M filters. The first filter was chosen as it has substantial overlap with the MUSE wavelength range (Table 1), which was required to perform the astrometric correction, whereas the other two filters allowed us to inspect the morphology of the nebular emission with a higher spatial resolution than provided by MUSE, in particular to aid in the identification of the SNRs (Section 3.2).

Finally, we also retrieved the longest available *Chandra* observation of NGC 1313 X-1 in order to inspect for the presence of nearby X-ray sources (see Section 3.2) associated with the

identified SNRs. We reprocessed these observations using the script `chandra_repro` using CIAO version 4.12 and CALDB 4.9.3. Table 1 provides a summary of all the data used in this work.

The optical counterpart of NGC 1313 X-1 was identified by Yang et al. (2011), which is depicted in the *HST* image in Figure 2. To identify the position of the counterpart in the MUSE cube, we used the *HST* image taken in the ACS/F555W filter to correct the astrometry of the cube and register it to the *HST* coordinates (Figure 2 left). To do so, we used the python package `mpdaf` (Piqueras et al. 2017) to integrate the MUSE cube in wavelength space, weighting each wavelength by the ACS/F555W filter throughput in order to generate a MUSE image in the F555W filter (central wavelength of  $5360 \text{ Å}$  with a bandwidth of  $360 \text{ Å}$ ). Then we used the task `adjust_coordinates` from the same package to run an autocorrelation function between the F555W MUSE and the *HST* images. The maximum of the autocorrelation function was used to shift the cube coordinates relative to the *HST* image and register its coordinates to this reference image. The resulting alignment is shown in Figure 2 and showed excellent agreement with the *HST* image. We considered the uncertainty on the position of the counterpart in the cube to be the nominal *HST* PSF added in quadrature to the pixel scale of MUSE ( $0.2''$ ). We fitted a 2D Gaussian profile to the optical counterpart in the *HST* image to determine the PSF FWHM =  $0.110 \pm 0.003''$ . Thus, the  $3\sigma$  uncertainty of the position of the optical counterpart in the MUSE cube was found to be  $\sim 0.61''$ . We note that the counterpart was not clearly detected in this MUSE image (but see Section 3.7).

### 3. Data analysis and results

#### 3.1. Line maps

In order to derive physical quantities from the main nebular lines, we used the publicly available code CAMEL<sup>3</sup> which is described in Epinat et al. (2012). CAMEL performs pixel-by-pixel Gaussian line fitting to derive flux and kinematic maps for each fitted line. We enhanced the signal-to-noise ratio (S/N) of the faint lines in the cubes by applying a 2D spatial Gaussian smoothing with FWHM = 2 pixels as the spatial resolution of the cube (PSF FWHM  $\sim 1''$ ) was well above the pixel scale of MUSE ( $0.2''$ ). A single Gaussian component was chosen to fit the lines, and CAMEL was run in five independent spectral cuts so the continuum could be easily modelled with a one degree polynomial in each cut. The only exception to this was the  $\text{H}\beta$  line that presented some Balmer absorption (see the dipping structure around the  $\text{H}\beta$  in Figure 1) that we took into account using a Gaussian absorption line together with a zero-degree polynomial to model the continuum. We found that the relative differences in  $\text{H}\beta$  flux between the approach where the continuum was modelled with a one degree polynomial and the approach taking into account the Balmer absorption were 1–50% (10th and 90th percentiles). Cuts in the spectral space were performed around the  $\text{H}\beta$  line, both [O III] lines, the [O I] $\lambda 6300$  line, the [N II]- $\text{H}\alpha$  complex, and finally one for the [S II] doublet. In each case we assumed the same line width for each pair of forbidden lines and the same line-of-sight velocity for the whole set of lines fitted in each cut.

The dispersion maps were corrected for instrumental broadening by subtracting the instrumental line spread function (LSF) FWHM in quadrature. In order to estimate the LSF FWHM, we computed the median and the standard deviation of the 10th per-

<sup>2</sup> <https://hla.stsci.edu/>

<sup>3</sup> <https://gitlab.lam.fr/bepinat/CAMEL>



**Table 1.** Log of the observations used in this work.

Telescope	Detector	ObsID	Date	Band	Exposure ks
<i>Chandra</i>	ACIS-S	2950	2002-10-13	0.3–10 keV	19.9
<i>HST</i>	ACS/WFC/F555W	hst_9796_01_acs_wfc_f555w	2003-11-17	4777–6017 Å	1.16
<i>HST</i>	WFC3/UVIS/F657N	hst_13773_15_wfc3_uvis_f657n	2015-02-24	6503–6628	1.5
<i>HST</i>	WFC3/UVIS/F547M	hst_13773_15_wfc3_uvis_f547m	2015-02-24	5108–5821	0.55
VLT	MUSE	ADP.2019-12-08T00:33:13.185	2019-10-17	4750-9350 Å	1.4
VLT	MUSE	ADP.2019-11-29T11:13:19.106	2019-10-16	4600–9350 Å	1.4

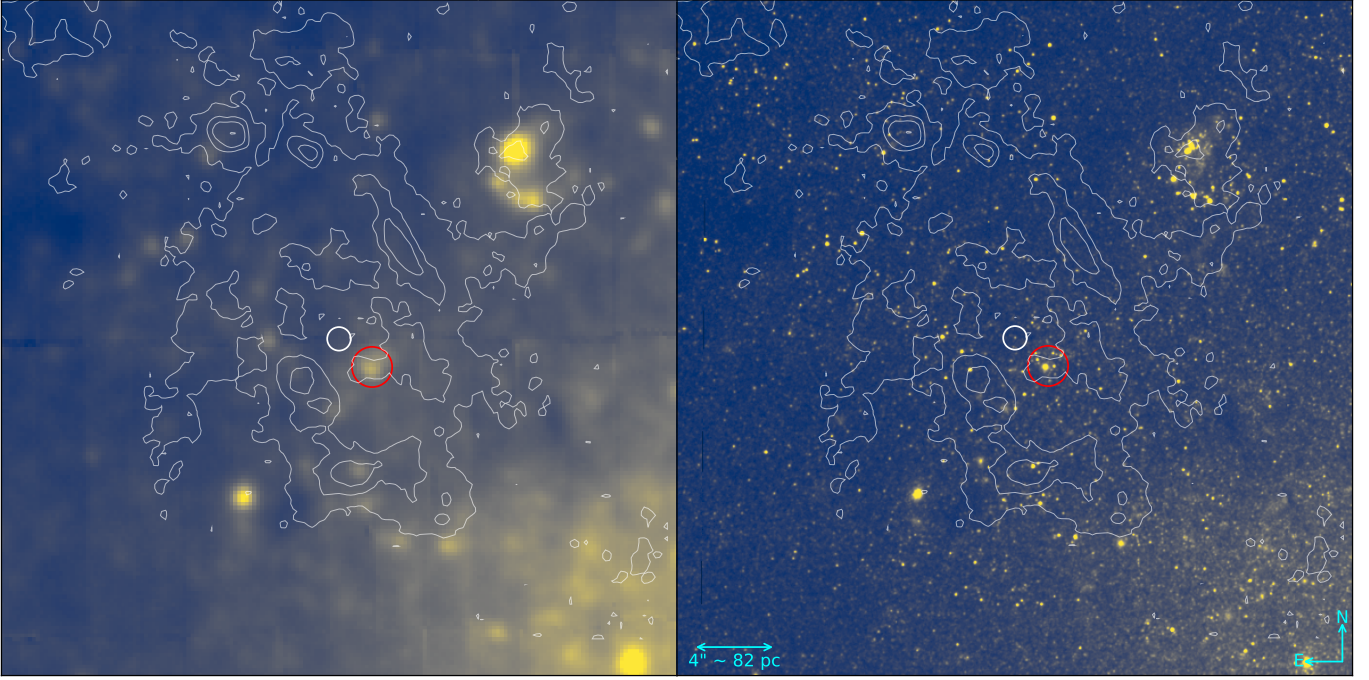


**Fig. 2.** Comparison between the (left) MUSE equivalent *HST*/ACS/F555W bandwidth and (right) *HST* images of the field around NGC 1313 X-1, after astrometric correction of the MUSE cube. The white circle in both images is 0.61'' in radius and shows the  $3\sigma$  uncertainty on the position of the ULX NGC 1313 X-1 in the MUSE cube. The position of the optical counterpart of NGC 1313 X-1 determined by Yang et al. (2011) can be seen on the *HST* image. The red circles indicate a bright star of a young cluster of massive stars (Ryon et al. 2017) to aid the comparison between the images. The contours show the flux of the [O I]  $\lambda 6300$  line (see Figure 5). Both images have the same orientation and show a region of  $30'' \times 30''$ .

centile FWHM of the dispersion maps produced by CAMEL for all the lines we measured. We additionally included the sky line at [O I]  $\lambda 6300$ , which was present throughout the spatial extent of the cube at its rest-frame wavelength. We only considered lines with  $S/N > 5$  to avoid introducing noise in the calculation. Table 2 reports the determined FWHM for the different lines along with the number of pixels from the dispersion map used in the calculation whereas Figure 3 shows a comparison with the parametrisation from Bacon et al. (2017) (see their Equations 7 and 8) for cube 1. The results for cube 2 were similar, and we do not report them for brevity.

The discrepancy found in the  $H\beta$  line might be due to the stellar absorption around this wavelength, affecting the estimation of its FWHM. The discrepancy between the other lines' FWHM values and the parametrisation of Bacon et al. (2017) is unclear. The parametrisation from Bacon et al. (2017) was derived by fitting the sky lines from a combined cube composed of 25-minute exposures totalling 10–37h with a specific observation pattern, where the field was rotated by  $90^\circ$  between exposures, an observing strategy far more complex than our single-exposure data

cubes. It is possible that the recipe derived by Bacon et al. (2017) might not be suited for our more simplistic case. We decided to focus only the FWHM of the [N II]- $H\alpha$  and [S II] lines, which showed good agreement with the parametrisation proposed by Bacon et al. (2017). We corrected the observed FWHM using our own estimation of the LSF FWHM, although the results are unchanged if instead we used the values obtained from Bacon et al. (2017).

The resulting line-of-sight and dispersion maps were more severely affected by the invalid pixels and noise present in the cubes in comparison with the flux maps. We therefore decided to use the information from cube 2 to improve them. As stated in Section 2, because the spatial distribution of the noise is unique to each cube, we found that we could improve the S/N of these maps by averaging the information obtained from cube 1 and cube 2. For the velocity maps, we further noted that the [N II]- $H\alpha$  and [S II] were consistent with each other, both spatially and numerically (the median and the standard deviation of the velocity differences between the two maps were  $-0.09 \pm 5$  km/s). We therefore decided to combine the information from the [N II]- $H\alpha$

**Table 2.** Results from the instrumental LSF FWHM estimation (see text for details). For the forbidden doublets only one line is shown as the same FWHM value was assumed.

Line	FWHM <sup>a</sup> Å	N <sup>b</sup>
H $\beta$	2.1 $\pm$ 0.5	2289
[O I] $\lambda$ 6300 <sup>†</sup>	2.20 $\pm$ 0.08	2880
[O I] $\lambda$ 6300	2.05 $\pm$ 0.09	2734
[O III] $\lambda$ 5007	2.5 $\pm$ 0.2	3101
H $\alpha$	2.55 $\pm$ 0.06	3276
[N II] $\lambda$ 6583	2.4 $\pm$ 0.1	3276
[S II] $\lambda$ 6716	2.54 $\pm$ 0.08	3276

**Notes.** <sup>(a)</sup> Average and standard deviation of the pixels used. <sup>(b)</sup> Number of pixels from the dispersion map used. <sup>(†)</sup> Sky line

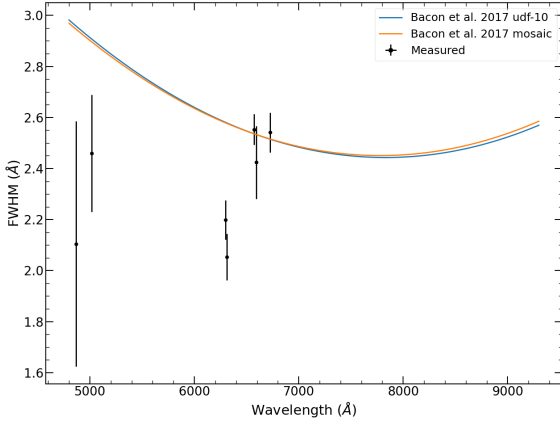


**Fig. 3.** Estimated FWHM (see text for details) compared to the parametrisation of Bacon et al. (2017). The FWHM estimated from the data cube does not show a good agreement with the parametrisation of Bacon et al. (2017) towards the blue part of the spectrum.

and [S II] maps from cube 1 and cube 2 in order to create an average map of these lines. The [O III] and [O I] $\lambda$ 6300 maps were also produced by averaging cubes 1 and 2. We similarly averaged the maps from the H $\alpha$ , [S II] $\lambda$ 6716, and [N II] $\lambda$ 6583 lines for the dispersion maps to obtain a smoother map as the maps showed again good consistency (the median and standard deviation of the differences between the H $\alpha$  and [S II] $\lambda$ 6716 maps were 13 $\pm$ 12 km/s, with the same values found for the differences between the H $\alpha$  and [N II] $\lambda$ 6583 maps). In this case we did not use the information from cube 2 as it was considerably affected by noise and did not provide any significant improvement.

The resulting maps for the line flux, dispersion and line-of-sight velocity are shown in Figures 5, 6, and 7 for some of the nebular lines with the best S/N. Pixels with a line detection S/N below 5 have been masked. Figure 4 shows a composite image of the H $\alpha$ , [O III] $\lambda$ 5007, and [S II] $\lambda$ 6716 lines. For the line-of-sight velocity maps, we subtracted the median value measured from the map after excluding the central parts of the bubble in order to reflect the local velocities more closely. This value was found to be 25 km/s, which is in good agreement with the estimated 30 km/s based on the measurements from Ryder et al. (1995) in Section 1.

The right panel of Figure 6 shows some regions of interest that will be discussed throughout the paper, and in particular in Sections 3.5 and 4.1. These were obtained by fitting 2D Gaussian ellipsoidal profiles to the [O I] $\lambda$ 6300 flux map, except for SNR

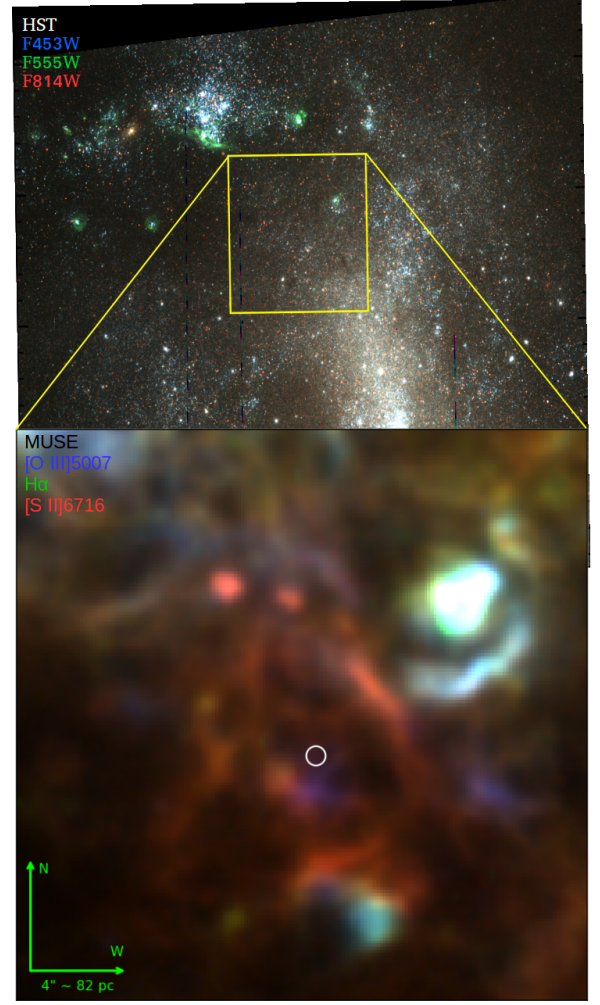


**Fig. 4.** (Top) Composite *HST* image showing F435W (Blue), F555W (Green) and F814W (red) ACS/WFC images downloaded from the HLA archive (ObsID hst\_9796\_01\_acs\_wfc\_f814w\_f555w\_f435w). The yellow square shows the region shown in the MUSE image in the bottom panel. (Bottom) MUSE RGB image of the nebula around NGC 1313 X-1 corresponding to the yellow square in the *HST* image, showing fluxes in H $\alpha$  (green channel), [O III] $\lambda$ 5007 (blue channel) and [S II] $\lambda$ 6716 (red channel) lines.

1 for which we used the H $\alpha$  map instead (see Section 3.4) and a circular Gaussian given its apparently symmetric profile. The radii of the regions were set equal to their respective FWHMs obtained, with the exception of regions 5, 6, and 7. For the first two we reduced the sizes obtained to avoid overlapping between them, whereas region 7 was simply determined visually. The integrated fluxes of these regions and the bubble are quoted in Table 3, while the sizes are given in Table 5. The two bright [S II] and [O I] $\lambda$ 6300 northernmost blobs are likely two SNRs coincidentally close to the ULX bubble, as we explain in Section 3.2. We describe first the regions concerning the interaction of the ULX with the interstellar medium (ISM).

The H $\alpha$ , [O I] $\lambda$ 6300, and [S II] $\lambda$ 6716 flux maps clearly reveal an elongated bubble in the south-west–north-east direction, 452  $\times$  266 pc in size (highlighted in the right panel of Figure 6 in cyan). The ULX is roughly at 1.2'' from the centre of the ellipsoidal shape marked by the bright [O I] $\lambda$ 6300 regions, corresponding to a physical distance of 25 pc.

Figure 6 shows that the lines are broadened just inside the edges marked by the [O I] $\lambda$ 6300 and [S II] $\lambda$ 6716 flux maps (see

**Table 3.** Observed fluxes of the different nebular lines relative to H $\beta$ , integrated in each of the regions highlighted in the right panel of Figure 6. Uncertainties are given at the  $1\sigma$  level by adding the uncertainty on each pixel in quadrature.

Line	SNR 1	SNR 2	Region 3	Region 4	Region 5	Region 6	Region 7	Bubble
H $\beta$ ( $10^{-15}$ ergs s $^{-1}$ cm $^{-2}$ )	1.5 $\pm$ 0.1	0.95 $\pm$ 0.08	2.1 $\pm$ 0.1	3.2 $\pm$ 0.2	2.4 $\pm$ 0.1	2.2 $\pm$ 0.1	1.7 $\pm$ 0.1	24.1 $\pm$ 0.4
[O III] $\lambda$ 4959	0.698 $\pm$ 0.002	0.713 $\pm$ 0.003	0.500 $\pm$ 0.002	0.589 $\pm$ 0.001	0.707 $\pm$ 0.002	0.386 $\pm$ 0.002	0.470 $\pm$ 0.002	0.550 $\pm$ 0.001
[O III] $\lambda$ 5007	2.175 $\pm$ 0.010	2.156 $\pm$ 0.011	1.543 $\pm$ 0.007	1.799 $\pm$ 0.006	2.143 $\pm$ 0.008	1.154 $\pm$ 0.006	1.449 $\pm$ 0.008	1.674 $\pm$ 0.002
[O I] $\lambda$ 6300	0.414 $\pm$ 0.002	0.433 $\pm$ 0.002	0.455 $\pm$ 0.001	0.474 $\pm$ 0.001	0.722 $\pm$ 0.002	0.770 $\pm$ 0.002	0.417 $\pm$ 0.002	0.496 $\pm$ 0.001
[N II] $\lambda$ 6548	0.191 $\pm$ 0.001	0.192 $\pm$ 0.001	0.207 $\pm$ 0.001	0.232 $\pm$ 0.001	0.276 $\pm$ 0.001	0.252 $\pm$ 0.001	0.220 $\pm$ 0.001	0.227 $\pm$ 0.001
H $\alpha$	3.614 $\pm$ 0.005	3.718 $\pm$ 0.004	3.490 $\pm$ 0.002	3.688 $\pm$ 0.002	3.555 $\pm$ 0.002	3.741 $\pm$ 0.002	3.687 $\pm$ 0.003	3.580 $\pm$ 0.001
[N II] $\lambda$ 6583	0.610 $\pm$ 0.006	0.610 $\pm$ 0.005	0.646 $\pm$ 0.003	0.732 $\pm$ 0.003	0.850 $\pm$ 0.004	0.794 $\pm$ 0.003	0.691 $\pm$ 0.004	0.711 $\pm$ 0.001
[S II] $\lambda$ 6716	1.304 $\pm$ 0.003	1.284 $\pm$ 0.004	1.374 $\pm$ 0.002	1.387 $\pm$ 0.002	1.522 $\pm$ 0.002	1.804 $\pm$ 0.002	1.305 $\pm$ 0.003	1.388 $\pm$ 0.001
[S II] $\lambda$ 6731	0.954 $\pm$ 0.002	0.920 $\pm$ 0.002	0.962 $\pm$ 0.001	0.976 $\pm$ 0.001	1.079 $\pm$ 0.001	1.263 $\pm$ 0.001	0.924 $\pm$ 0.001	0.980 $\pm$ 0.001

particularly the strong broadening FWHM  $\sim 100$  km/s towards the south near region 6, north-east near region 3, and east to the NGC 1313 X-1 near region 5). This is a telltale sign that the gas is being shocked in these regions and defines the limit of the interaction of the ULX with the surrounding medium. The maximum FWHM measured in these regions (3, 4, 5, 6, and 7) were in the 90–130 km/s range (Table 5 gives the maximum FWHM values measured in each of the regions of interest). Instead, the [O III] $\lambda$ 5007 flux map shows slightly different morphology, with a brighter region just south of the ULX position, also clearly visible in Figure 4 as a light blue blob.

The line-of-sight velocity ( $V_{\text{los}}$ ) fields (Figures 7) show a structure roughly contained inside the [O I] $\lambda$ 6300 contours, with  $V_{\text{los}}$  about 30–40 km/s higher than those of the surrounding gas, indicating that the gas inside the bubble is being dynamically perturbed by the ULX via outflows. This is clearly seen in the combined [N II]-H $\alpha$  and [S II] and [O III] $\lambda$ 5007  $V_{\text{los}}$  fields. This is illustrated more clearly in Figure 8, which is a close-up of the two maps around the ULX position. We also note the distinct structure of the two maps, which suggests that the [O III] $\lambda$ 5007 map is tracing different gas compared to the combined H $\alpha$ [N II][S II] map. The combined [N II]-H $\alpha$  and [S II] velocity fields show peak velocities of  $\sim 20$  km/s, whereas the surrounding gas shows slower velocities reaching at most  $\sim 0$  km/s with a typical  $1\sigma$  uncertainty of  $\sim 1$  km/s. The [O III] $\lambda$ 5007 shows higher velocities reaching up to  $\sim 35$  km/s, whereas the gas in the outer regions of the bubble has velocities of at most  $\sim 5$  km/s. The typical  $1\sigma$  uncertainty of the maps of the individual cubes here is slightly higher (by  $\sim 4$  km/s). The [O I] $\lambda$ 6300 map shows a somewhat similar structure to the H $\alpha$ [N II][S II] maps, with two distinct regions north and south from the ULX, albeit with considerably higher noise.

Finally, we note that the dispersion map in the [O I] $\lambda$ 6300 line reveals some strong broadening (uncorrected FWHM  $\gtrsim 200$  km/s) at the position of NGC 1313 X-1 (see Figure 17). We note, as stated in Section 2, that the exact value of the instrumental-corrected FWHM is uncertain. Nevertheless, because this broadening is coincident with the source position, we used it in Section 3.7 to extract a spectrum of the optical counterpart.

### 3.2. Supernova remnants in disguise

Figures 4 and 5 reveal two compact spots bright in the [S II] and [O I] $\lambda$ 6300 lines, located north of the ULX (labelled SNR 1 and SNR 2 in the right panel of Figure 6). These are at  $\sim 12''$  and  $9.8''$  from the ULX position, corresponding to a physical distance of  $\sim 250$  pc and  $200$  pc, respectively. Here we find intrinsic FWHM values reaching up to  $\sim 166$  km/s in the combined H $\alpha$ , [N II],

and [S II] dispersion map<sup>4</sup>, the highest values in the whole nebula. The broadening and the strong [S II] and [O I] $\lambda$ 6300 lines implies that the gas is also being shocked in these regions. However, its association with the ULX is unclear as its distance is extreme even for ULX standards (cf. 150 pc from S26 NGC 7793; Pakull et al. 2010), whereas its round morphology (notably for SNR 1) argues against a jet or wind excitation, for which we would likely expect an arc-shaped structure instead (cf. regions 3 and 7). A face-on view could still make an arc shape appear circular, but considering its already large projected distance this is highly unlikely. Recently, these regions have been identified as SNRs by Kopsacheili et al. (2021) based on their [S II]/H $\alpha$  > 0.4 ratios, a common diagnostic used to identify SNRs. However, most of the gas inside the bubble also shows [S II]/H $\alpha$  > 0.4 (see Section 3.3) and in fact many ULX bubbles were initially misclassified as SNRs based on this diagnostic (e.g. Matonick & Fesen 1997). In this regard, Urquhart et al. (2019) offers an interesting historical discussion on the early identification of several ULX bubbles as SNRs to which we refer the interested reader. For this reason we decided to investigate the nature of these regions to assess whether they were related to the ULX activity. Here we show that their identification as SNRs is nonetheless likely to be robust as it is based on a more detailed imaging and spectral analysis.

In order to inspect the morphology of the diffuse emission of these regions in more detail, we retrieved a *WFC3/UVIS/F657N* image (which isolates the H $\alpha$  + [N II] lines) from the HLA archive, together with a *WFC3/UVIS/F547M* image for the continuum subtraction. The details of these observations are reported in Table 1. In order to isolate more precisely the H $\alpha$  + [N II] emission, we subtracted the continuum emission as measured from the F547M image. More specifically, we took into account the bandwidths of the different filters by measuring the ratio between the intensities in these two images in four different circular regions of 4–5" containing stars and no obvious diffuse emission. The median of these ratios was used as a rescale factor to the continuum image before subtracting it from the narrow-band image (prior to this, the images were aligned as explained below). The subtracted image (Figure 9) shows that the emission from SNR 1 is almost spherical, with an angular radius of  $\sim 0.85''$  (17.5 pc), confirming what had been hinted at from the MUSE H $\alpha$  image, and strongly supporting its identification as a SNR (Kopsacheili et al. 2021). Based on the morphology alone, the situation might be less clear for SNR 2 due to the low S/N of the diffuse emission, but its shape might also be suggestive of a

<sup>4</sup> The colour scale of the figure does not reflect such high values owing to the chosen scaling, which is meant to aid the visualisation of the other areas.



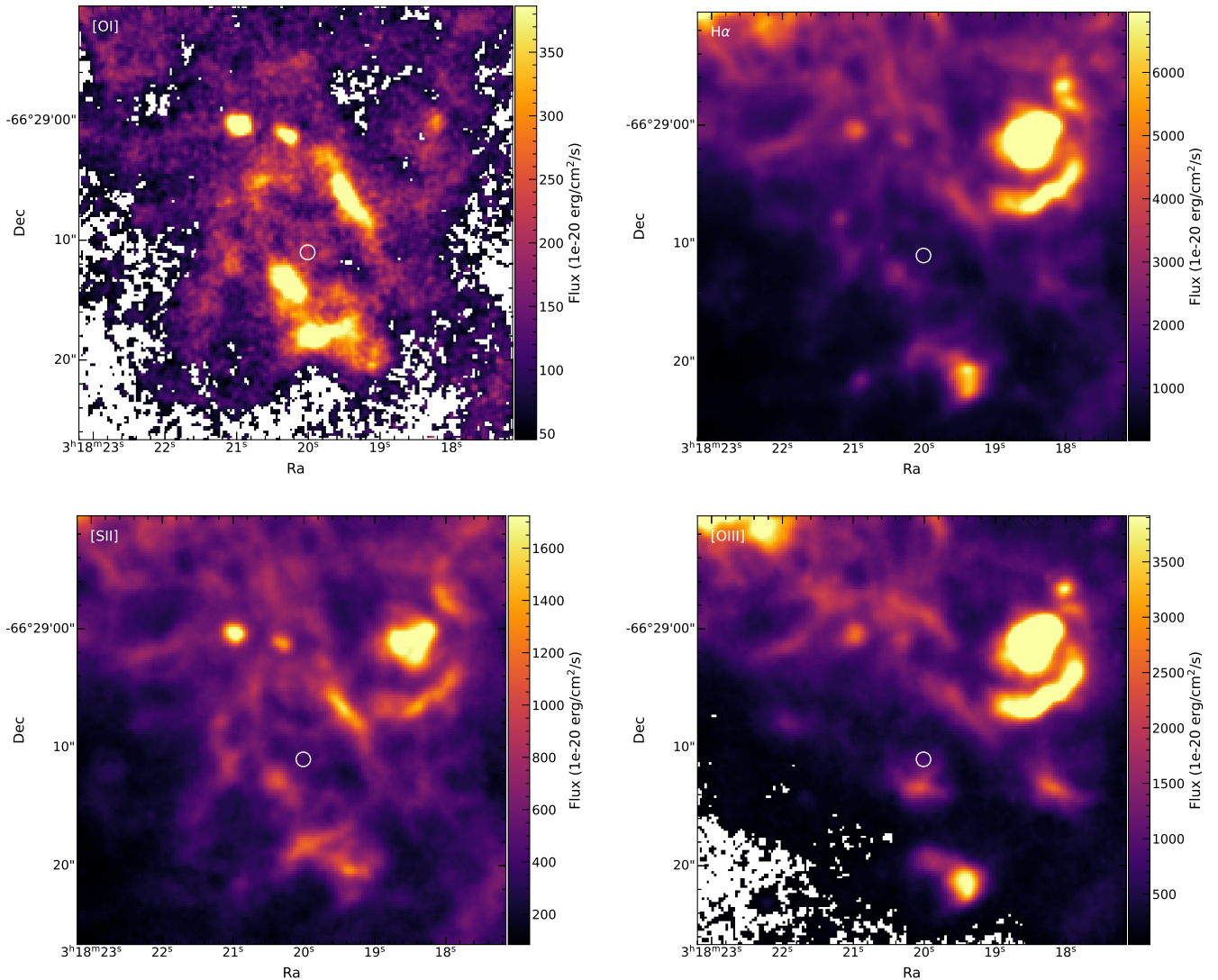


**Fig. 5.** Flux maps for [O I] $\lambda$ 6300 (top left), H $\alpha$  (top right), [S II] $\lambda$ 6716 (bottom left), and [O III] $\lambda$ 5007 (bottom right). The small white circle indicates the position of NGC 1313 X-1 and its uncertainty (see text for details). The scale and direction are the same as in Figure 4.

SNR. We also note the brighter emission from these two regions compared to the rest of the nebula.

We also present spectra of the two SNRs averaged over each of the regions. These are shown in Figure 10 along with the average spectrum from region 4 for comparison. The resemblance between the two SNR spectra and the presence of several emission lines typically seen in SNRs (Fesen & Hurford 1996) strengthens the association of the SNR 2 as a SNR. A detailed analysis of these spectra is beyond the scope of the present paper, but based on the similarity between SNR 1 and SNR 2 we believe there is enough evidence to support the classification of SNR 2 as a SNR. Even if this is not the case, we note that our main conclusions remain unaffected. These spectra also illustrate the well-known difficulty in distinguishing ULX bubbles from SNRs (e.g. Pakull & Grisé 2008), and provide further evidence for region 4 being excited by shocks.

For completeness, we also decided to inspect the *Chandra* images for any evidence of associated X-ray emission which could strengthen their classification as SNRs. To this end, we used archival ObsID 2950 as it had the longest exposure time and the smallest PSF distortion around the ULX, owing to its

off-axis angle of 2.317', compared to 6.884' for the other two observations available in the archives (ObsIDs 3550 and 3551). The details of this observation is also reported in Table 1.

To precisely align the optical and X-ray images to a common reference frame, we matched the sources detected in both wavelengths to the *Gaia* DR2 source catalogue (Gaia Collaboration et al. 2018). For the three *HST* images (F555W, F547M, and F657N filters) we used the tool *tweakreg* from the *astrodrizzle* package<sup>5</sup>, which allows both source detection and cross-matching. We tested different sets of parameters and decided to use a detection threshold of  $75\sigma$  and to restrict the number of sources used in the matching stage to the 846 brightest sources (set to twice the amount of *Gaia* sources in the F555W field of view). This was in order to restrict the matching stage to the brighter sources more readily detected by *Gaia*. After cross-matching each of the images, we allowed the task to subsequently incorporate the new sources (not included in the original reference *Gaia* catalogue) detected in the previous images to build a larger reference catalogue for the next image.

<sup>5</sup> <https://drizzlepac.readthedocs.io/en/latest/index.html>

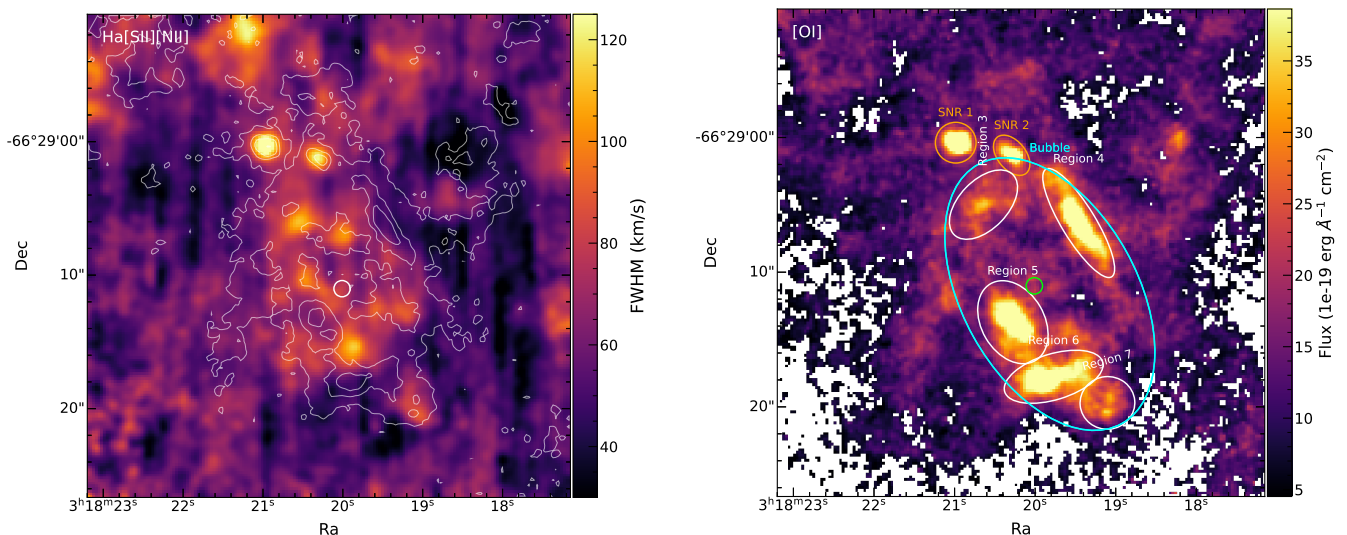


**Fig. 6.** Dispersion and flux maps of the region around NGC 1313 X-1. (left) The dispersion map of the average of the  $H\alpha$ ,  $[N II]\lambda 6853$ , and  $[S II]\lambda 6716$  lines, corrected for instrumental broadening (contours as in Figure 2). The map has been smoothed with a Gaussian kernel with  $\sigma = 1.5$  pixels. (right)  $[O I]\lambda 6300$  flux map showing some regions discussed throughout the paper, the ULX bubble (cyan), and the coincidentally close SNRs (orange). The position of the ULX is indicated with a green circle.

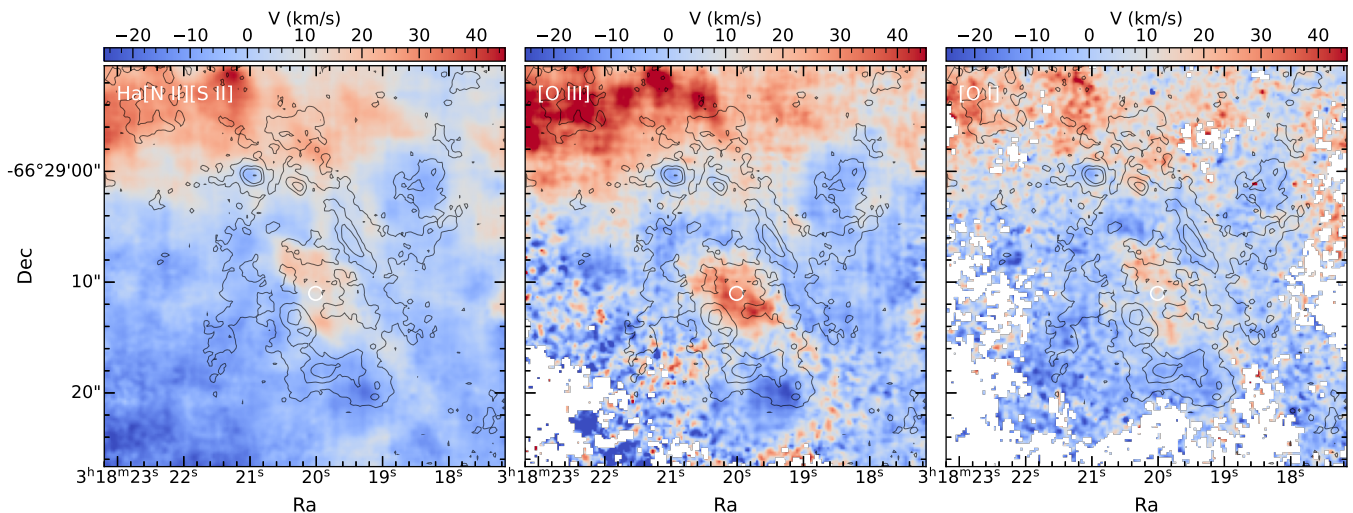


**Fig. 7.** Line-of-sight velocity maps over the system velocity of NGC 1313 ( $\sim 470$  km/s) for the combined  $[N II]-H\alpha$  and  $[S II]$  lines (left),  $[O III]$  (middle), and  $[O I]\lambda 6300$  (right). An offset of 25 km/s (the median value estimated from the whole map after excluding the central bubble) has been subtracted to reflect more closely the local velocities, which is in good agreement with the 30 km/s estimated at the position of NGC 1313 X-1 based on the values given by [Ryder et al. \(1995\)](#) (see Introduction). The scale is the same in all panels, the contours as in Figure 6.

Owing to its larger field of view the F555W image was used first, followed by the F547M image, and lastly the F657N due to its narrower filter. We found 85, 33, and 307 matches for the F555W, F547M, and F657N filters respectively, resulting in rms residuals all below 0.007".

For the *Chandra* images we used the *ciao* task *wavdetect* on the 0.5–7 keV band for source detection. A faint ( $\sim 13$  net counts) source north-east of the ULX is detected<sup>6</sup> (Figure 9), with a  $1\sigma$  statistical uncertainty on the position of  $\delta$  R.A. = 0.36" and  $\delta$  DEC = 0.19". To examine whether this source could be the X-ray counterpart of SNR 1, we used the task *wcsmatch* with an initial search radius of 4" to match the X-ray sources to the

*Gaia* catalogue. After an initial transformation, an iterative process discards all matches with radii above a certain value and continues to update the solution until no more matches are discarded. We visually inspected the resulting matches obtained for different radii and settled for a value of 0.6". This resulted in five matches: two background AGN, two foreground stars (one used in the work of [Yang et al. 2011](#) for this same correction), and the supernova remnant SN1978K (e.g. [Kuncarayakti et al. 2016](#)). The rms residuals were 0.16". Adding all the uncertainties in quadrature, the final  $3\sigma$  uncertainty on the position of the source is  $\delta$  R.A. = 1.2" and  $\delta$  DEC = 0.8". Based on the  $3\sigma$  confidence contour depicted in Figure 9, we rule out the association of the X-ray emission with SNR 1.

<sup>6</sup> This source is CXOU J031821.2–662858 in the work of [Mineo et al. \(2012\)](#), identified as a high-mass X-ray binary.



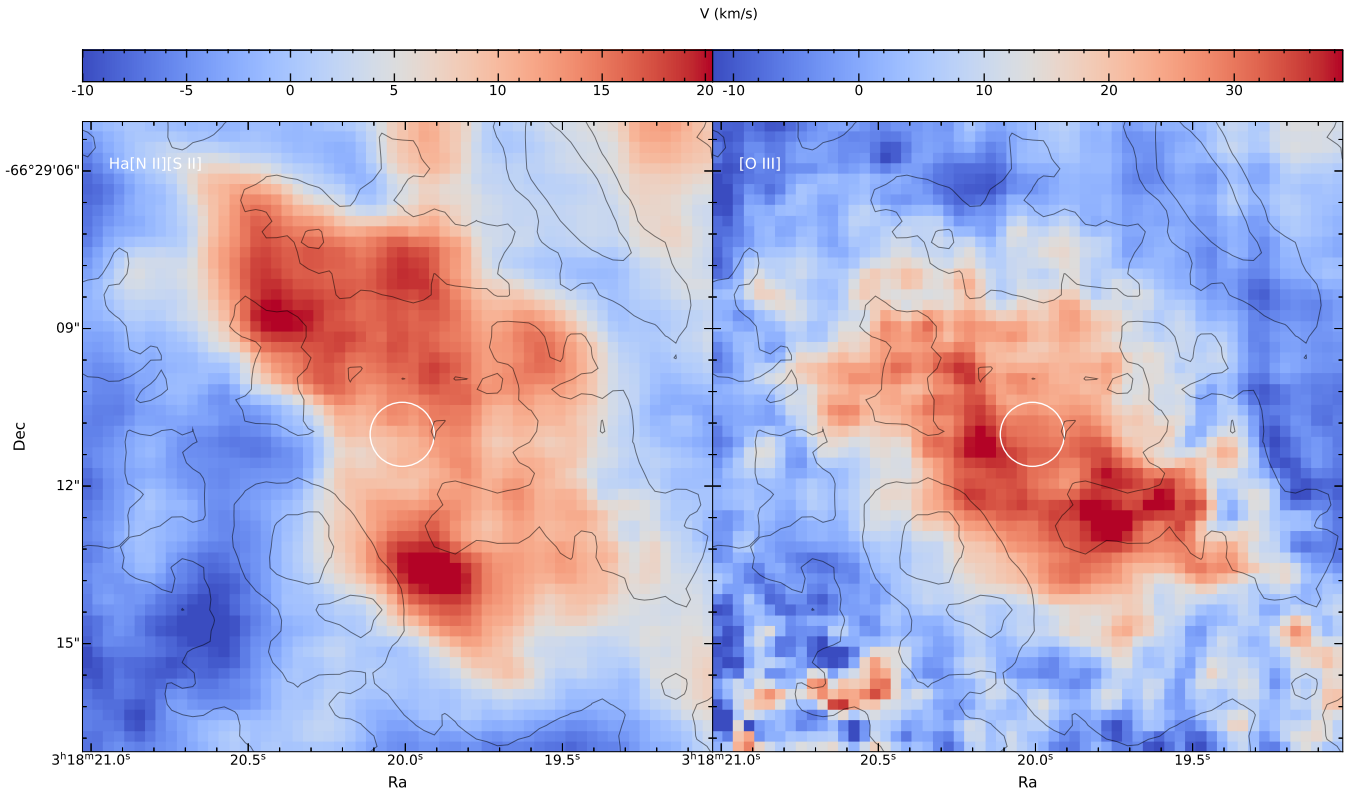


**Fig. 8.** Close-up view of the velocity maps for the  $H\alpha$ [N II][S II] (left) and [O III] maps (right). Note the difference in scale between the two maps. The position of the ULX is indicated with a white circle. Contours as per Figure 7.

### 3.3. Baldwin–Phillips–Terlevich diagrams

In order to study the physical conditions of the gas around NGC 1313 X-1, we exploited MUSE access to the main nebular lines to derive spatially resolved [O III] $\lambda$ 5007/ $H\beta$  versus [N II]/ $H\alpha$ , [O III] $\lambda$ 5007/ $H\beta$  versus [S II]/ $H\alpha$ , and [O III] $\lambda$ 5007/ $H\beta$  versus [O I]/ $H\alpha$  Baldwin–Phillips–Terlevich (BPT) diagrams (Baldwin et al. 1981; Veilleux & Osterbrock 1987). These diagrams use the flux ratios of the Balmer lines to the forbidden lines to distinguish regions of gas ionised by stars (HII regions) from regions ionised by hard X-ray emission and/or shocks (AGN regions and LINER). To classify the regions based on these line ratios, a theoretical and empirical classification scheme is commonly used based on the works of Kewley et al. (2001), Kauffmann et al. (2003), and Kewley et al. (2006). For instance, Kewley et al. (2001) derived the theoretical maximum ratios expected from regions photoionised solely by stars, using photoionisation and stellar synthesis population codes. This line is termed the maximum starburst line, and it is used to differentiate between HII regions from intermediate regions (where hard X-ray radiation and/or shocks start to contribute) and/or AGN-dominated regions (mainly ionised by shocks and/or hard X-ray radiation). However, these early works were based purely on line ratios of integrated spectra of galaxies, resulting in mixing of various components. By using IFU data from the MaNGA galaxy survey, Law et al. (2021) recently refined these classification schemes by combining spatially resolved line ratios and the kinematic information provided by the dispersion along the line of sight of the  $H\alpha$  line. This classification results in a cleaner separation between the different components compared to early works and we therefore made use of it to derive the BPT diagrams shown in Figure 11. We also note that these diagrams are essentially in-

dependent of the exact reddening correction since the line ratios employed are sufficiently close in wavelength such that the correction can be safely ignored.

The diagrams clearly highlight that most of the pixels around the ULX are classified as AGN, LINER or intermediate, indicating that the ULX contributes heavily to the ionisation budget of the surrounding environment. The [N II]/ $H\alpha$  BPT diagram is more sensitive to metallicity. For this reason, at low oxygen abundances ( $\log(O/H) + 12 \lesssim 8.4$ ), AGN regions become difficult to distinguish from classical HII regions, mostly owing to the dependency of the [N II] $\lambda$ 6583/ $H\alpha$  ratio with metallicity (Kewley et al. 2013). We show in Section 3.6 that the metallicity around NGC 1313 X-1 is  $\log(O/H) + 12 \approx 8.1$ –8.4. This likely explains why many of the regions classified as AGN–LINER in the other two BPT diagrams are found in the HII–intermediate region in the [N II] $\lambda$ 6583/ $H\alpha$  diagram. Nevertheless, this diagram is useful because the pixels classified as AGN likely trace the hard EUV/X-ray radiation from the source, as the hardness of the ionisation field tends to increase the [O III] $\lambda$ 5007/ $H\beta$  ratio (Kewley et al. 2013), given the relatively high ionisation potential needed to doubly ionise oxygen. Thus, the [N II] $\lambda$ 6583/ $H\alpha$  BPT diagram essentially offers a map of the regions strongly excited by EUV/X-rays from the ULX.

The other two diagrams show a central roughly circular region slightly offset to the south from the position of NGC 1313 X-1, where the gas is classified as AGN and LINER. This classification is also observed in regions SNR 1 and SNR 2. Comparison of these diagrams with the kinematic data and the [O I] $\lambda$ 6300 and [S II] $\lambda$ 6716 flux maps (see Section 3.1) suggest that the lightly coloured regions found at the boundary of the AGN and LINER regions mostly highlight regions ex-

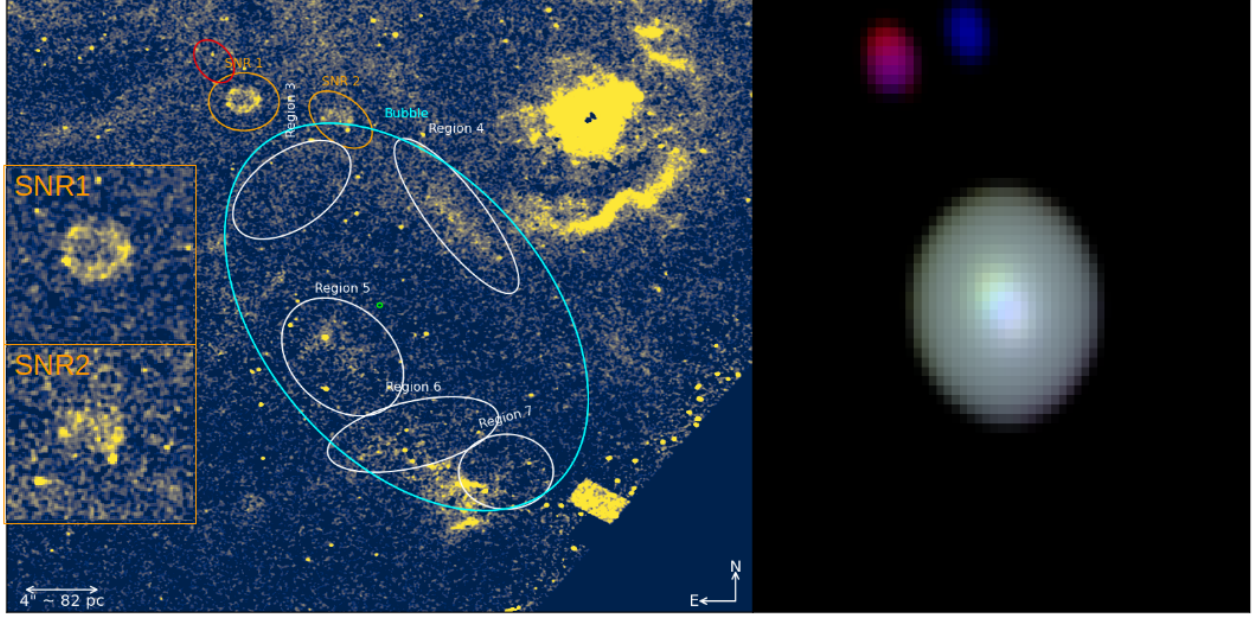


**Fig. 9.** The field around NGC 1313 X-1 in optical and X-rays. The left panel shows the *HST* continuum-subtracted WFC3/UVIS/F657N ( $H\alpha$  + [N II]) image. The WFC3/UVIS/F547M image was used for the continuum approximation and the position of NGC 1313 X-1 is indicated by a green circle. The red ellipse shows the  $3\sigma$  contour confidence level of the easternmost source with red-ish colours in the *Chandra* image. The same regions from Figure 6 are also shown, and the insets show close-ups of the two SNRs, as indicated. The right panel shows a R,G,B = 0.5–1.2 keV, 1.2–2 keV, 2–7 keV *Chandra* image showing the same field. Both images show a  $32'' \times 32''$  field centred around the ULX and have been smoothed with 2 pixel Gaussian kernel.

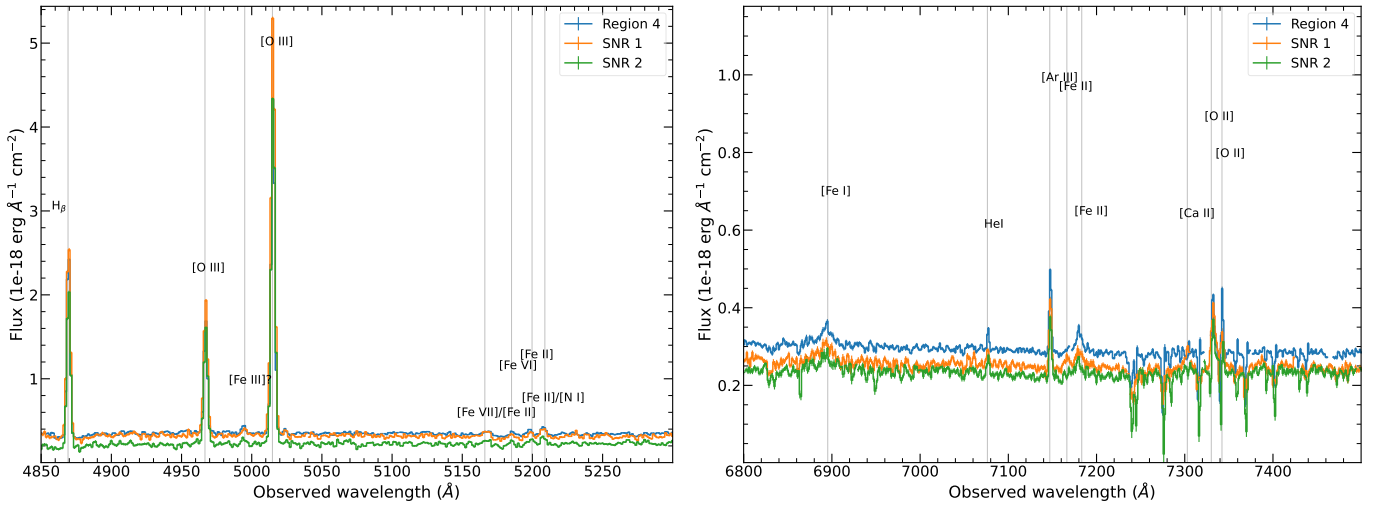


**Fig. 10.** Average spectra extracted from regions SNR 1, SNR 2, and region 4 in Figure 6 showing the spectral bands in the ranges 4850–5300 Å (left) and 6800–7500 Å (right). The thin vertical lines show the expected transitions at the redshift of NGC 1313 based on the line catalogue from Fesen & Hurford (1996). The spectra have been smoothed with a Gaussian kernel of 2.5 Å. Small gaps mask some pixels having negative values due to low S/N.

cited by shocks. To further illustrate this point, we show the [O I] $\lambda 6300/H\alpha$  BPT diagram coloured based on the FWHM values from Figure 6 in Figure 13, whereas in Figure A.1 in the Appendix the same result is shown, but for each of the regions highlighted in the right panel of Figure 6. We can clearly see that pixels with largest FWHM values are concentrated close to the intermediate boundary, between the AGN and LINER regions. These correspond mainly to regions SNR 1 and SNR 2 and regions close to 3 and 4 where strong broadening is seen, which all have values  $-1 < \log([O I]\lambda 6300/H\alpha) < -0.75$ .

Regions 5 and 6 include some of the strong broadening seen in these areas, but the ratios where FWHM is strongest are in-

stead pushed to higher [O I] $\lambda 6300/H\alpha$  ratios ([O I] $\lambda 6300/H\alpha > 0.25$  or  $\log([O I]\lambda 6300/H\alpha) > -0.6$ ) compared to the other regions (Figure A.1), most notably for region 6. These regions also show a clear dependence with distance to the ULX, with the pixels closer to the ULX showing high  $\log([O III]\lambda 5007/H\beta) \gtrsim 0.25$  as a result of the higher excitation by the ULX, whereas pixels further from the ULX are again found at the boundary between AGN, LINER and intermediate regions. We note in particular how the [O III] $\lambda 5007/H\beta$  ratio is much lower in region 6, whereas the [O I] $\lambda 6300/H\alpha$  value has increased. These pixels with [O I] $\lambda 6300/H\alpha$  are located to the south and east of the region classified as LINER in the [S II] $\lambda 6717/H\alpha$  or [O I] $\lambda 6300$  di-

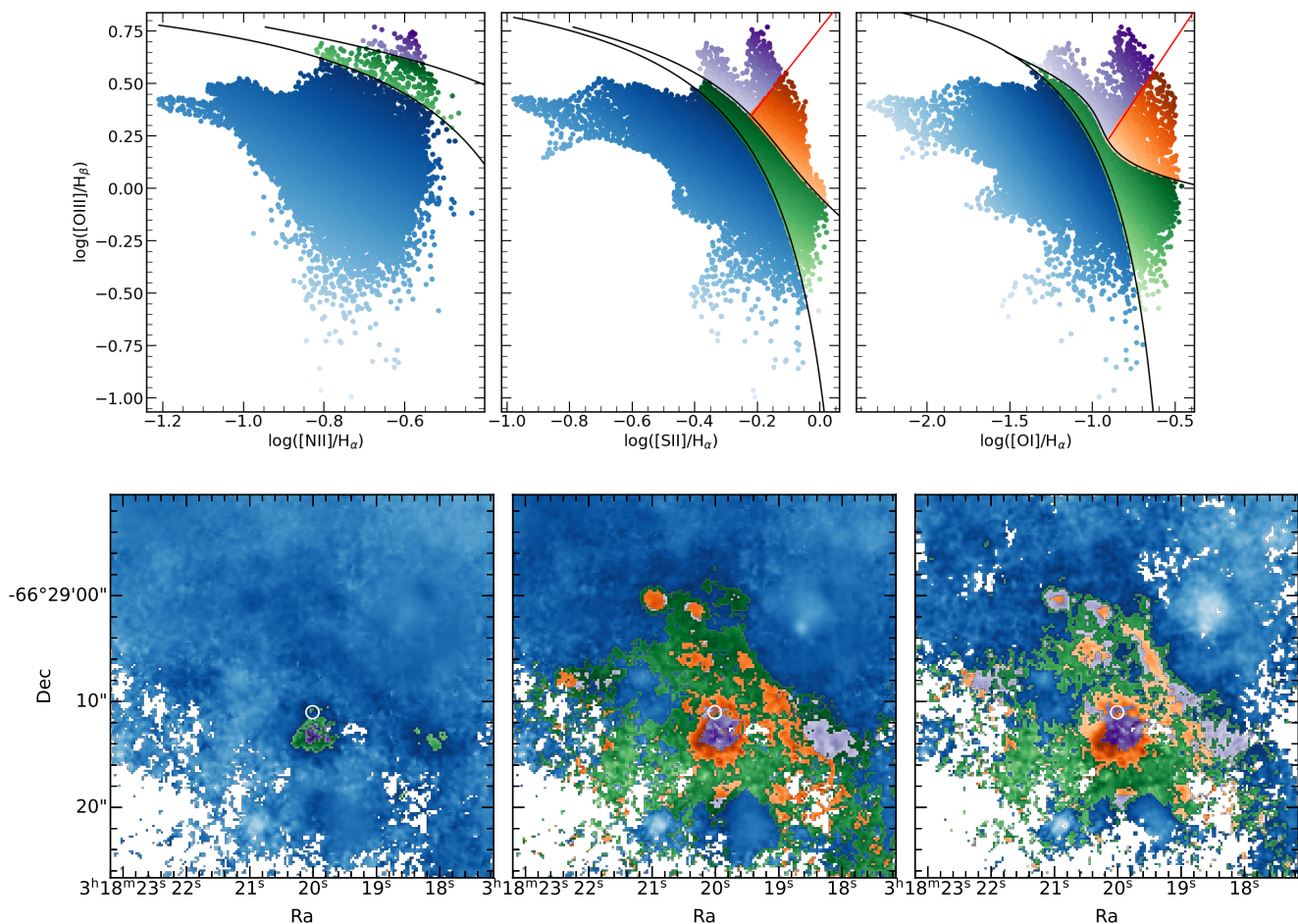


**Fig. 11.** Results of the spatially-resolved BPT diagrams using the classification proposed by Law et al. (2021). Regions classified as HII, intermediate, AGN, and LINER are shown in blue, green, purple, and orange, respectively. The top panels show the classification of each pixel based on the line ratios, whereas the bottom panels show their corresponding location. Each pixel has been colour-coded proportionally to the sum of the x and y values in all panels to aid the visualisation and localisation of each pixel in the bottom panels.

agrams. To illustrate this in more detail, we show in Figure 12 the  $[\text{O III}]\lambda 5007/\text{H}\beta$  contours over the  $[\text{O I}]\lambda 6300/\text{H}\alpha$  image. This shows the presence of a highly ionised zone (in this case traced by the high  $[\text{O III}]\lambda 5007/\text{H}\beta$  ratio) surrounded by regions of bright forbidden transitions of neutral atoms (here traced by the  $[\text{O I}]\lambda 6300/\text{H}\alpha \gtrsim 0.25$  ratio). This is consistent with the expectation of an X-ray ionised nebula (Halpern & Grindlay 1980), in very good agreement with the weakly ionised region reported by Pakull & Mirioni (2002). Therefore in regions 5 and 6 we are likely seeing a mixture of shock and X-ray ionised gas. In region 7 we note that some of the pixels include the contribution from the stellar cluster located east of it, which explains the array of values found in the HII region, but again we observe some the pixels located at the AGN–LINER–intermediate boundary. In summary, we see that the environment of the ULX shows indications of being ionised by both EUV/X-ray radiation and shocks. While we do observe some pixels with FWHM  $\sim 80\text{--}120\text{ km/s}$  within the HII region in Figure 13 (see the yellow coloured data points at  $-1.5 < \log([\text{O I}]\lambda 6300/\text{H}\alpha) < -1.25$ ) associated with the northernmost region in Figure 13, we can rule out these as being due to shocks because of their position in the BPT diagrams.

### 3.4. Comparison with the MAPPINGS libraries

BPT diagrams are a powerful tool used to separate regions excited by stars from those excited by EUV/X-ray radiation and/or shocks (LINER and AGN regions). However, these diagrams cannot cleanly separate regions excited by shocks from EUV/X-ray radiation, although in Sections 3.1 and 3.3 we saw that the kinematic data can help in this discrimination. For this reason, it is often valuable to complement these diagrams with the predictions from radiative shock libraries. Here we chose to do so with the up-to-date set of pre-run shock-ionisation MAPPINGS V models (Sutherland et al. 2018) compiled by Alarie & Morisset (2019), which is an extension of the MAPPINGS III models (Allen et al. 2008) to a wider range of abundances from the work of Gutkin et al. (2016). With this analysis we can also attempt to provide an independent estimate of the shock velocities in the bubble ( $v_{\text{shock}}$ ), which will be relevant to evaluate the mechanical power needed to inflate the bubble (Section 4.1) as well as the explosion energy of the SNRs (Section 4.2).

We show in Section 3.6 that the metallicity around NGC 1313 X-1 is  $12 + \log(\text{O}/\text{H}) \approx 8.1\text{--}8.4$ . We therefore considered models for SMC ( $\log(\text{O}/\text{H}) + 12 = 8.03 \pm 0.10$ ) and LMC abundances ( $\log(\text{O}/\text{H}) + 12 = 8.35 \pm 0.6$ ) (Russell & Dopita 1992)



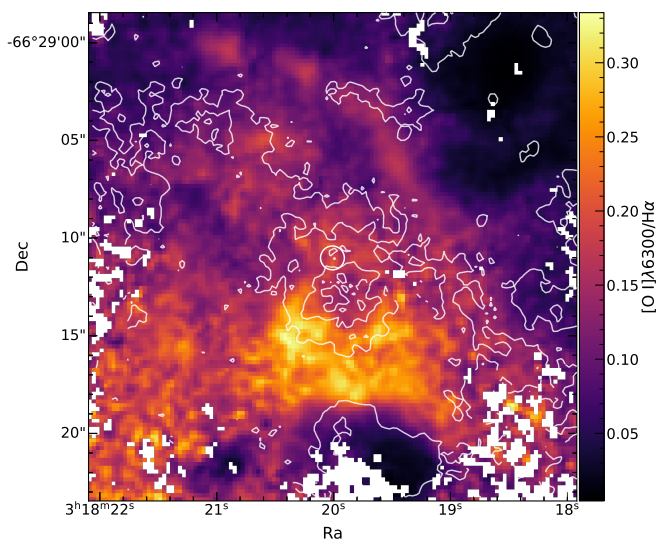


**Fig. 12.** [O I]λ6300/Hα map with the [O III]λ5007/Hβ contours overlaid in white showing a region of 25''x25'' around the ULX (white circle). Extended emission with high [O I]λ6300/Hα ratios is seen south to the peak of the [O III]λ5007/Hβ indicating X-ray excitation.

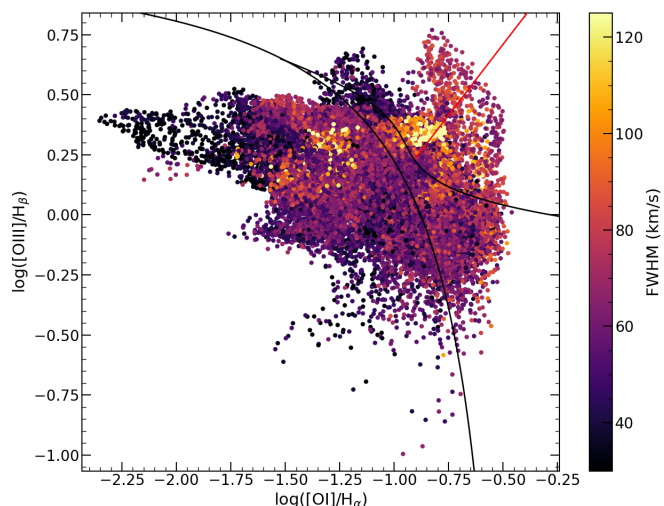


**Fig. 13.** Spatially resolved [O III]λ5007/Hβ vs [O I]λ6300/Hα BPT diagram coloured as a function of the intrinsic FWHM of the Hα line. The solid lines show the classification scheme proposed by Law et al. (2021), as in Figure 11.

from the updated Allen et al. (2008) set, which have the closest set of abundances to our estimates. From the Gutkin et al. (2016) abundances, we considered four abundances to match roughly the observed range:  $Z = 0.002, 0.004, \text{ and } 0.01$  which correspond approximately to  $12 + \log(\text{O}/\text{H}) = 7.91, 8.21, \text{ and } 8.61$ , respectively<sup>7</sup>. We also consider a representative range of pre-shock magnetic fields given in Figure 14. Using the Gutkin et al. (2016) models, for which the pre-shock density ( $n_{\text{ISM}}$ ) can be varied logarithmically in the  $1\text{--}10000\text{ cm}^{-3}$  range, we found that the best match to the data was given for  $n_{\text{ISM}} = 1\text{ cm}^{-3}$ . Models with  $n_{\text{ISM}} = 10\text{ cm}^{-3}$  were also acceptable, but mostly had the effect of making the line ratios less sensitive to variations in the pre-shock magnetic value than  $v_{\text{shock}}$ . Therefore, the range of ve-

locities found were roughly the same as those recovered for  $n_{\text{ISM}} = 1\text{ cm}^{-3}$ . We also note that our estimates from Section 3.5 suggest  $n_{\text{ISM}} \lesssim 5\text{ cm}^{-3}$  even for velocities as low as  $\sim 100\text{ km/s}$ , and thus we considered only models with  $n_{\text{ISM}} = 1\text{ cm}^{-3}$ . The predicted line ratios from the libraries are compared with our line ratio estimates in Figure 14.

From the [S II]/Hα and [O I]λ6300/Hα diagrams, it is clear that velocities in excess of  $v_{\text{shock}} \gtrsim 150\text{ km/s}$  are needed to produce the observed line ratios close to the AGN, LINER, and intermediate boundaries, especially for the range of metallicities that more closely match our estimates (Section 3.6). The LMC or  $12 + \log(\text{O}/\text{H}) = 8.24$  set of abundances with velocities  $v_{\text{shock}} \sim 200\text{ km/s}$  or the SMC abundances with slightly higher velocities  $v_{\text{shock}} \sim 250\text{ km/s}$ , seem to provide a good match to our data (cf. Figure A.1). It is also clear that values with  $\log([\text{O III}]\lambda 5007/\text{H}\beta) \gtrsim 0.45$  cannot be explained by shocks alone as they either require shock velocities  $\gtrsim 300\text{ km/s}$ , which can be ruled out by our kinematic data, or a set of abundances with abnormally high metallicity (cf. Figure 3.6), also ruled out by our estimates. Therefore, pixels at the uppermost right region of the BPT diagrams seem consistent with mainly EUV/X-ray excitation. A similar argument can be made about the pixels with the highest [O I]λ6300/Hα ratios seen in regions 5 and 6. This is in line with the analysis presented in Sections 3.1 and 3.3, where it was shown that shocked regions are instead close to the AGN–LINER–intermediate boundary delimitation. Considering the [N II]/Hα diagram, it seems that the best match to the data would be given by the set of LMC abundances, in good agreement with our metallicity estimates (Section 3.6). The set of points with  $\text{FWHM} \gtrsim 120\text{ km/s}$  seen in Figure 13 closer to the AGN, LINER and intermediate boundaries is clustered around  $-0.8 < \log([\text{N II}]/\text{H}\alpha) < -0.6$  and  $0.25 < \log([\text{O III}]\lambda 5007/\text{H}\beta) < 0.5$  in this diagram, which again would suggest  $175\text{ km/s} < v_{\text{shock}} < 200\text{ km/s}$ . In summary, the line ratios with values at rightmost part of the [O I]λ6300/Hα and [S II]/Hα diagrams or with very high ( $\gtrsim 0.45$ ) values of  $\log([\text{O III}]\lambda 5007/\text{H}\beta)$  ratio cannot be explained by shocks, suggesting that these are regions excited by EUV/X-ray radiation. Instead, regions closer to the AGN–LINER–intermediate boundary line are closely matched by shocks with velocities in the  $\sim 165 < v_{\text{shock}} < 225\text{ km/s}$  range.

It is often worth comparing these estimates with the kinematical data. In this regard, Soria et al. (2021) provides an interesting discussion on how to relate the measured line FWHMs to the shock velocity in their Appendix, to which we refer the interested reader for more details. Briefly, if we are observing the projected central region of a thin spherically expanding bubble, we expect to observe a velocity distribution function  $f_c = \frac{1}{2}[\delta(v - v_{\text{exp}}) + \delta(v + v_{\text{exp}})]$ , where  $v_{\text{exp}}$  is the expanding velocity of the bubble. For radiative shocks,  $v_{\text{exp}} = v_s$  (Dewey 2010), leading to  $v_{\text{shock}} = 0.425\text{ FWHM}$ . Considering that in reality we observe a finite region with a range of velocities instead of a delta function and that some gas lags behind the shock, Soria et al. (2021) suggest that  $v_{\text{shock}} = 0.47\text{ FWHM}$  is a more appropriate relationship. Another possibility is to take a spectrum of the entire bubble instead of observing a finite region. In this case, assuming there is a single expansion velocity for the whole bubble, the observed velocity distribution is a uniform distribution  $f_T = \frac{1}{2} v_{\text{exp}}$ , which leads to  $v_{\text{shock}} = 0.735\text{ FWHM}$ . Given the morphology of the nebula, we considered only a circular region at the centre of the cyan ellipse in the right panel of Figure 6 with radius  $7.5''$  ( $\sim 150\text{ pc}$ ), roughly delimited by regions 4, 5, and 6. Here we measured a maximum FWHM of  $127\text{ km/s}$  and a mean of  $70\text{ km/s}$  from the mean Hα, [N II], and [S II] map. Assuming the case of a spherically thin expanding nebula, this would

<sup>7</sup> We have assumed a dust-to-metal mass ratio of 0.1 for the conversion (see Gutkin et al. 2016).

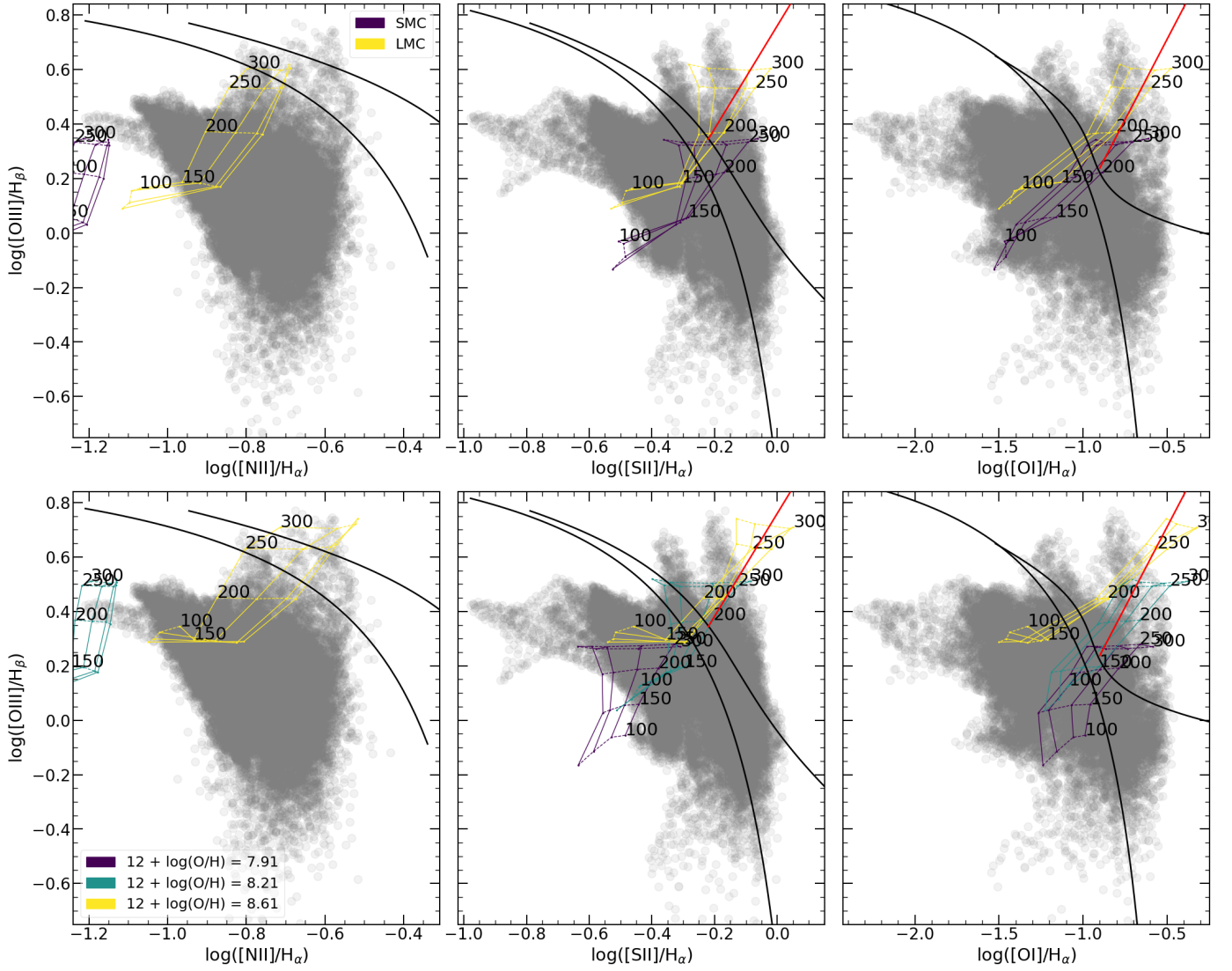


**Fig. 14.** Comparison between the theoretical ratios predicted by the radiative shock libraries compiled by [Alarie & Morisset \(2019\)](#) for the precursor and shock models from abundances from [Allen et al. \(2008\)](#) (top) and abundances from [Gutkin et al. \(2016\)](#) (bottom) and the observed values. Each colour shows the predictions for a set of abundances (see text for details). Each line connects the predictions for shock velocities ranging from 100 to 300 km/s in steps of 50 km/s, as indicated. The models for a given velocity are connected by a dashed line, indicating the effect of varying the pre-shock magnetic field for  $10^{-4}$ , 1, 3.23, and  $5 \mu\text{G cm}^{3/2}$ . The grey data points and the black solid lines correspond to the data and region delimitations from Figure 11.

suggest  $v_{\text{shock}} \sim 55$  km/s using either of the two estimates. However, such slow  $v_{\text{shock}}$  values are at odds with the measured line ratios, as we show in Section 3.4. We also note that a radial expansion does not appear to be supported by the  $V_{\text{los}}$  maps, which shows instead some sort of outflowing gas emanating from the ULX (see the trough in the velocity field at the ULX position in Figure 8).

It is also possible in our case, given the high shock velocity inferred from the line ratios, that the FWHM we are measuring is a blend of the broadened line from the shock and the narrow component from the photoionised precursor, only broadened by thermal Doppler effect. We note that the presence of the shock precursor is strongly supported by the fact that this component is needed to match the line ratios in the LINER and AGN regions. Given the moderate resolution of MUSE (instrumental FWHM of  $\sim 116$  km/s at  $6560 \text{ \AA}$ ), it is likely that we cannot resolve these two components. If the narrow component from the precursor dominates the emission, this can result in a narrower

Gaussian fit to the blended line profile than if the shocked component could be resolved and modelled alone. We can see some evidence in support of this phenomenon in SNR 1 (Figure 6), where the FWHM measured with a single-Gaussian component was the strongest and where we found the strongest fit residuals, which could indicate the presence of a more complex line profile. We focused on the  $H\alpha$  line as it is the one with the strongest S/N, and extracted a spectrum from the region shown in Figure 6, determined by fitting a 2D Gaussian, profile as explained in Section 3.1.

We performed Gaussian fits of the  $H\alpha$  line using the `python` package `lmfit`<sup>8</sup> considering one or two Gaussian components. The continuum was modelled using a constant around the line centroid. The best-fit parameters for one and two components are shown in Table 4. Figure 15 shows the best-fit two-Gaussian model component, with the corresponding residuals for one and two Gaussian components shown in the panels below. We also

<sup>8</sup> <https://lmfit.github.io/lmfit-py/>

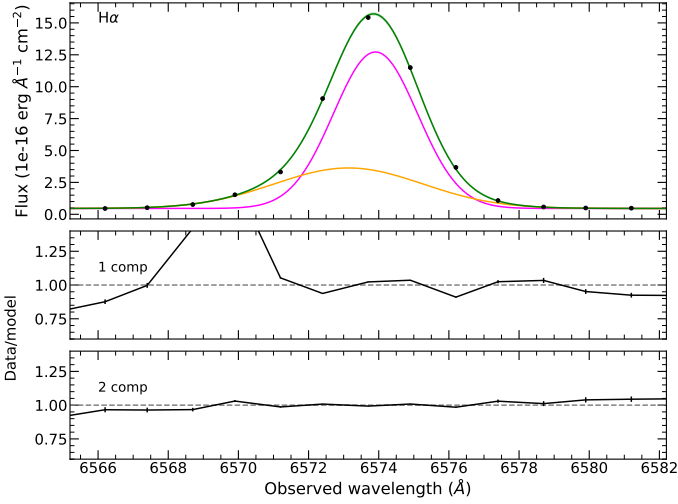


**Fig. 15.** Results of the fitting process to the integrated  $H\alpha$  line of the SNR 1 region (Figure 6). (top) Best fit (green solid line) to the integrated  $H\alpha$  emission from region SNR 1 using two Gaussian components (shown in pink and yellow). The lower panels show the ratio plots of one- and two-component fits.

tried more complex profiles such as a Lorentzian or a Voigt profile, but they yielded worse fits than the single-Gaussian model.

The single-Gaussian component deviates strongly from the line profile at the blue wing of the line profile, suggesting the presence of a second broad component. In agreement with the above argumentation, the second broad component alone is broader ( $\text{FWHM} = 196 \pm 8$  km/s) than the single-Gaussian model component ( $\text{FWHM} = 98 \pm 6$  km/s). The former FWHM value is in turn much closer to the shock velocities inferred from the MAPPINGS libraries. We conclude that it is possible that the narrow component of the precursor causes the FWHM of the lines to be underestimated. It must also be noted that a one-to-one correspondence between  $v_{\text{shock}}$  and FWHM is not expected given that the FWHM might not necessarily sample the direction of maximum expansion. Considering the uncertainties associated with relating FWHM to the shock velocity, we decided to rely on the shock velocities inferred from MAPPINGS rather than from the kinematic data.

Based on the different positions of the selected regions in the BPT diagrams (Figure A.1) we assigned them a shock velocity depending on the typical values found for the SMC, LMC and  $12 + \log(\text{O}/\text{H}) = 7.91, 8.21$  abundances. These are shown in Table 5. We also report in Table 5 the maximum FWHM found in the selected regions. There is clear trend in the sense that regions with higher FWHM show higher shock velocity values as derived using the line ratios. This suggests that the estimated shock velocities based on the MAPPINGS libraries are reasonable. The shock velocities found are typically a factor of  $\sim 1.4$  higher than the measured FWHMs. Similar factors were also found by Dopita et al. (2012) in the study of the microquasar NGC 7793 S26. Given that region 6 does not show much overlap with the line ratios predicted by the MAPPINGS libraries, notably where FWHM is strongest (Figure A.1) owing to the likely contribution from X-ray ionisation (Section 3.3), we simply assigned it  $v_{\text{shock}} = 1.4 \text{ FWHM}$ . We also note that the differences between the FWHM values and the shock velocities inferred from the line ratios we found are much smaller than in previous works such as Urquhart et al. (2018) or Soria et al. (2021), who found  $v_{\text{shock}}$  based on the line ratios to be  $\gtrsim 5$  FWHM. We

note however that as stated earlier these values are less certain for regions 5 and 6 given the likely contribution from X-ray radiation.

### 3.5. ISM Density estimates

A key physical quantity necessary to estimate the energetics of the bubble (see Section 4) and that of the SNRs (Section 4.2) is the pre-shock density of the ISM ( $n_{\text{ISM}}$ ). This quantity can be estimated using Equation 3.4. from Dopita & Sutherland (1996), who provide a relationship between the surface brightness of the  $H\beta$  line in the shock,  $v_{\text{shock}}$ , and  $n_{\text{ISM}}$ :

$$f_{H\beta\text{shock}} = 7.44 \times 10^{-6} v_{100}^{2.41} \times \frac{n_{\text{ISM}}}{\text{cm}^{-3}} \text{ erg s}^{-1} \text{ cm}^{-2}. \quad (1)$$

Here  $v_{100}$  is the shock velocity in units of 100 km/s. In cases where  $v_{\text{shock}} > 150$  km/s, the shock will create a photoionised precursor that needs to be taken into account (Dopita & Sutherland 1996). The same relationship as above but for the precursor term reads (their Equation 4.4.)

$$f_{H\beta\text{precursor}} = 9.85 \times 10^{-6} v_{100}^{2.28} \times \frac{n_{\text{ISM}}}{\text{cm}^{-3}} \text{ erg s}^{-1} \text{ cm}^{-2}; \quad (2)$$

combining the two equations,  $n_{\text{ISM}}$  can be expressed as

$$\frac{n_{\text{ISM}}}{\text{cm}^{-3}} = \frac{10^6 L_{H\beta}}{A(7.44 v_{100}^{2.41} + 9.85 v_{100}^{2.28})}, \quad (3)$$

where  $A$  is the surface area of the emitting region. The surface area of each region was estimated assuming a prolate ellipsoid (i.e. we assumed the shorter of the semi-axes for the third dimension of the ellipsoid). We estimated the density of the ISM for the two SNRs and the bubble, and for each of the elliptical regions shown in the right panel of Figure 6, where we found clear signs of shock excitation, as argued in Sections 3.1 and 3.3. We caution again that these estimates might be less robust for regions 5 and 6 given that a fraction of the  $H\beta$  luminosity might be produced by X-ray excitation. We return to this point in Section 4.1.

The integrated flux in the  $H\beta$  line map in each of the mentioned regions was corrected for reddening using the observed Balmer decrement map. To this end, we followed Momcheva et al. (2013), who provide a relationship between the observed Balmer decrement and the colour excess:

$$E(B - V) = \frac{-2.5}{k(H\beta) - k(H\alpha)} \times \log_{10} \left( \frac{(H\alpha/H\beta)_{\text{int}}}{(H\alpha/H\beta)_{\text{obs}}} \right). \quad (4)$$

Here we used the extinction curve of Calzetti et al. (2000) with  $R_v = 4.05$  to obtain  $k(H\beta) = 4.6$  and  $k(H\alpha) = 3.3$ . For the intrinsic  $H\alpha/H\beta$  ratio, the MAPPINGS libraries suggested values of  $\approx 2.95$ – $3.0$  for SMC and LMC abundances (see Sections 3.4 and 3.6) and for shock velocities  $v_{\text{shock}} = 175$ – $225$  km/s. We therefore assumed an intrinsic ratio  $H\alpha/H\beta = 3.0$  for the extinction correction.

The estimated  $n_{\text{ISM}}$  values are in overall good agreement with the  $0.1$ – $1 \text{ cm}^{-3}$  values typically found in other ULX bubbles (e.g. Pakull et al. 2005). In general the values found for all regions across the bubble are in good agreement, except for region 4 where the slightly higher  $n_{\text{ISM}}$  value might explain its higher surface brightness.



**Table 4.** Best-fit parameters to the integrated H $\alpha$  line of region SNR 1 (Figure 6 right panel) for one and two Gaussian components (uncertainties at the  $1\sigma$  level).

	Wavelength Å	$V_{\text{los}}^a$ km/s	FWHM km/s	Flux $10^{-15} \text{ erg cm}^{-2} \text{ s}^{-1}$
1 Component	6573.78 $\pm$ 0.07	31 $\pm$ 3	98 $\pm$ 6	5.2 $\pm$ 0.1
2 Components	6573.92 $\pm$ 0.03	38 $\pm$ 1	56 $\pm$ 5	3.7 $\pm$ 0.2
	6573.15 $\pm$ 0.09	3 $\pm$ 4	196 $\pm$ 8	1.7 $\pm$ 0.2

**Notes.** <sup>(a)</sup> Line-of-sight velocity over the galaxy redshift ( $z = 0.001568$ ).

**Table 5.** Measured and estimated quantities of interest for the regions shown in the right panel of Figure 6. All uncertainties are at the  $1\sigma$  level.

Region	$a^a$ arcsec	$b^b$ arcsec	Area <sup>c</sup> $10^{40} \text{ cm}^2$	$R^d$ pc	$\Sigma L_{\text{H}\beta}^e$ $10^{36} \text{ erg/s}$	$\langle E(B-V) \rangle^f$	FWHM <sup>g</sup> km/s	$v_{\text{shock}}^h$ km/s	$n_{\text{ISM}}^i$ $\text{cm}^{-3}$	$t^j$ $10^5 \text{ yr}$	$P_{\text{mec}}^j$ $10^{39} \text{ erg/s}$	$E^k$ $10^{51} \text{ erg}$
SNR 1	1.51	1.51	11.6	257 $\pm$ 6	6.37 $\pm$ 0.02	0.16 $\pm$ 0.06	166 $\pm$ 27	220 $\pm$ 25	0.5 $\pm$ 0.1	0.24–0.27	–	0.3–0.8
SNR 2	1.72	1.06	8.1	211 $\pm$ 5	4.64 $\pm$ 0.02	0.20 $\pm$ 0.08	136 $\pm$ 20	200 $\pm$ 25	0.7 $\pm$ 0.2	0.27–0.34	–	0.3–0.8
3	3.12	1.81	25.1	164 $\pm$ 9	8.35 $\pm$ 0.02	0.12 $\pm$ 0.08	119 $\pm$ 13	165 $\pm$ 25	0.6 $\pm$ 0.2	–	–	–
4	4.68	1.26	24.2	116 $\pm$ 1	15.25 $\pm$ 0.03	0.18 $\pm$ 0.08	110 $\pm$ 12	170 $\pm$ 25	1.1 $\pm$ 0.4	–	–	–
5	3.30	2.33	35.5	69 $\pm$ 3	10.66 $\pm$ 0.03	0.16 $\pm$ 0.07	110 $\pm$ 13	170 $\pm$ 25	0.5 $\pm$ 0.2	–	–	–
6	3.80	1.70	27.6	137 $\pm$ 5	11.16 $\pm$ 0.04	0.2 $\pm$ 0.1	130 $\pm$ 15	180 $\pm$ 25	0.6 $\pm$ 0.2	–	–	–
7	2.03	1.96	19.9	199 $\pm$ 8	7.90 $\pm$ 0.04	0.2 $\pm$ 0.1	100 $\pm$ 17	160 $\pm$ 25	0.8 $\pm$ 0.3	–	–	–
Bubble	11	6.5	318.6	134–227	105.6 $\pm$ 0.12	0.16 $\pm$ 0.1	130	170 $\pm$ 25	0.6 $\pm$ 0.2	4.6 $\pm$ 0.7–7.8 $\pm$ 1.2	19 $\pm$ 10–55 $\pm$ 30	~188–990

**Notes.** <sup>(a)</sup> Semi-major axis of the elliptical region. <sup>(b)</sup> Semi-minor axis. <sup>(c)</sup> Surface area of the ellipsoidal region, for which we assumed a radius equal to  $b$  for the third dimension (i.e. a prolate spheroid). <sup>(d)</sup> Average distance from the centre of the region to the average between the centre of the bubble and the position of the ULX. For the bubble we quote instead the semi-major and semi-minor axes. <sup>(e)</sup> Integrated extinction-corrected luminosity in the region. The error is propagated from the error flux map and takes into account the uncertainty on  $E(B-V)$ . We assumed a distance to NGC 1313 X–1 of 4.25 Mpc in the calculations of the luminosities. <sup>(f)</sup> Mean and standard deviation of  $E(B-V)$  in each region to provide some reference values, although the extinction correction was applied on a pixel-by-pixel basis. <sup>(g)</sup> Maximum FWHM measured in each region. The error is the typical spread in the region. <sup>(h)</sup> Shock velocity estimated from the observed line ratios in each region after comparison with the MAPPINGS libraries (see text for details). <sup>(i)</sup> Estimated age of the bubble or, in the case of the SNRs, time since the initial explosion. <sup>(j)</sup> Estimated average mechanical power required to inflate the bubble. <sup>(k)</sup> Estimated explosion energy in the case of an evolved SNR in the pressure-driven snowplough phase (see Section 4.2 for details).

### 3.6. Metallicity

The presence of shocks heavily affects abundances in nebulae (e.g. Peimbert et al. 1991) and requires specific modelling (Allen et al. 2008). Consequently, empirical metallicity diagnostics remain restricted to photoionisation zones, and are built with careful samples of reliable HII (or similar) regions. The most prevalent tools currently in use (e.g. Pérez-Montero 2017) are often based on temperature and density estimations originating from weak recombination lines (Osterbrock & Ferland 2006). However, these lines are either outside the observed bandpass of MUSE (e.g. the [O III] $\lambda$ 4363 and [S III] $\lambda$ 9532 lines) or are too weak to be detected above the continuum (e.g. [N II] $\lambda$ 5755). We therefore used the strong line method, through the  $S$  (empirical) calibration provided by Pilyugin & Grebel (2016), which only relies on strong lines (H $\beta$  [O III] $\lambda$ 4959,5007, [N II] $\lambda$ 6548,6584, and [S II] $\lambda$ 6717,6371), clearly detected in our data cube. More specifically, as suggested by the authors, we used two different calibrations (their Equations 6 and 7, respectively) for the upper ( $\log N_2 \geq -0.6$ ) and lower ( $\log N_2 < -0.6$ ) branches, where  $N_2 = ([\text{N II}]\lambda 6548 + [\text{N II}]\lambda 6584) / \text{H}\beta$  (see Pilyugin & Grebel 2016, for more details), to calculate  $12 + \log(\text{O}/\text{H})$ .

Because this method is only calibrated for HII regions, we restricted our analysis to the dynamically cold regions. We followed the principle used in Dors et al. (2017), who considered the cold–warm delimitation of the [S II]/H $\alpha$  BPT diagram of Kewley et al. (2006) (see Lara-López et al. 2021 for a similar approach). Here we also excluded the new intermediate delimitation of Law et al. (2021), as we have seen that this delimitation region is affected by the X-ray ionisation of the source (Sec-

tion 3.3). Hence we restricted the analysis to the regions strictly classified as HII.

Given that some of the line ratios involved in the metallicity computation are rather distant in wavelength, we corrected the corresponding fluxes for extinction using the methodology outlined in Section 3.5, this time adopting the theoretical value for Case B recombination of  $\text{H}\alpha/\text{H}\beta = 2.86$ , more suitable for HII-like regions (Osterbrock & Ferland 2006). The values obtained for  $E(B-V)$  in the regions of interest in this case are in the 0.15–0.8 range. The resulting metallicity map is shown in Figure 16.

We find a  $3\sigma$ -clipped median and standard deviation of  $12 + \log(\text{O}/\text{H}) = 8.18 \pm 0.04$ . These estimates are slightly below the values reported by Walsh & Roy (1997), who found that the metallicity in NGC 1313 followed a nearly flat profile with  $12 + \log(\text{O}/\text{H}) \approx 8.4 \pm 0.1$ . We note that in the bright HII regions created by the stellar cluster north-west and south of the ULX the metallicity is closer to the values reported by Walsh & Roy (1997) (purple areas in the map). Therefore, while some of these differences in metallicity are likely due to the difference in the reddening correction and the metallicity calibration used, it may be possible that the method we employed is less suitable for these diffuse regions. Nevertheless, a plausible range for the metallicity around NGC 1313 X–1 seems 8.1–8.4, which is in line with the estimates from the MAPPINGS libraries (Section 3.4). We can also confidently say that NGC 1313 X–1 was formed in a subsolar environment.

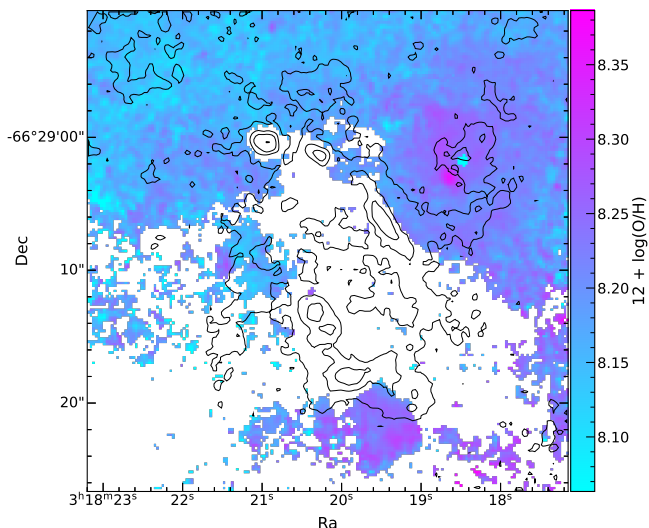


**Fig. 16.** Metallicity map around NGC 1313 X-1 only for those regions classified as HII regions (see text for details) based on the [S II]/H $\alpha$  vs [O III] $\lambda$ 5007/H $\beta$  BPT diagram (Figure 11). Contours as per Figure 2.

### 3.7. Optical counterpart

As stated earlier, the optical counterpart is not detected in the ACS/F555W equivalent MUSE image (Figure 2), nor in the white light MUSE image. The lowest Vega magnitude in any of the  $U$ ,  $V$ ,  $I$  filters reported by Yang et al. (2011) from analyses of the 2004 *HST* data was  $\sim 22.6$  in the  $U$  filter. The MUSE cube has a limiting AB magnitude of  $\sim 20.6$ , as determined by the automatic pipeline (Weilbacher et al. 2020), which translates to a  $\sim 20$  Vega magnitude. Thus, our sensitivity is too low to assess whether the optical counterpart has varied with respect to the 2004 observations. The counterpart might be additionally blurred due to the limited spatial resolution (PSF FWHM  $\sim 1''$ ) of the MUSE data cube.

However, while the counterpart is not detected, as stated in Section 3.1, we observed an enhancement of the width of the [O I] $\lambda$ 6300 line at the position of NGC 1313 X-1, with the FWHM reaching a peak value of 200 km/s, as stated in Section 3.1 (see Figure 17). We determined the peak and the FWHM of this enhancement by fitting a 2D Moffat profile to the region around the peak emission to select a suitable extraction region for the spectrum of the optical counterpart. We used a circular region centred at the peak with a  $\sim 0.5''$  radius for both semi-axes, as given by the estimated FWHM. We chose the background from an annulus centred at the source position to encompass some of the nebular emission. We set the inner radius to be equal to the source radius and the outer radius to 1.5'' in order to avoid the significantly brighter south-east rim of the nebula.

Figure 17 shows the background-subtracted spectrum around the H $\alpha$ -[N II] complex, which shows that the resulting spectrum is dominated by noise and is oversubtracted. There were no obvious features in the spectrum of the optical counterpart besides the sky residuals, suggesting that the emission is dominated by the nebular emission, which precluded us from characterising the optical counterpart.

## 4. Discussion

The simultaneous spectral and imaging capabilities of MUSE allowed us to analyse in detail the complex morphology of the

bubble around NGC 1313 X-1, first noticed by Pakull & Mirioni (2002). The nebula shows an indication of excitation by both shocks and EUV/X-rays. Shock excitation is seen at outer edges of the nebula close to the NGC 1313 X-1, revealed by the strong [O I] $\lambda$ 6300/H $\alpha$  and [S II]/H $\alpha$  ratios, together with the strong broadening (FWHM  $\gtrsim 100$  km/s) of the H $\alpha$ , [N II], and [S II] lines near those regions (see Figures 5, 6 and A.1). This strong broadening at the edges of the bubble is also seen in other ULX bubbles where the kinematics have been studied, such as those around NGC 1313 X-2 (Ramsey et al. 2006) and NGC 5585 X-1 (Soria et al. 2021). We have also seen that the gas in a region of  $\sim 7.5''$  around the ULX shows a high line-of-sight velocity compared to the surrounding gas (Figure 7). In particular, the mean H $\alpha$ [N II][S II] and [O III] velocity maps show two high-velocity regions with a trough at the source position (Figure 8), which argues against a radial expansion, which could be the case for a SNR. This strongly suggests that the gas inside the bubble is being dynamically perturbed by winds emanating from the ULX, creating the cavity around it. The strong broadening at the edges of the bubble is then thought to be an indication of the gas being decelerated at the shock front, strongly supporting that the bubble has been (and is being) inflated by a wind and/or jets. Therefore, these results provide direct and supporting evidence for the presence of powerful winds in NGC 1313 X-1, so far only revealed through X-ray spectroscopy (Walton et al. 2016; Pinto et al. 2016, 2020b). We show below that the estimated mechanical power of the wind in these previous works is in remarkable agreement with that estimated from the bubble. The elongated shape and the roughly diametrically opposite regions 3 and 7 (see in particular the [O I] $\lambda$ 6300 contours in Figure 6) might suggest that we are witnessing the activity of a jet. Follow-up radio observations would therefore be of great interest to confirm this. Given the clear evidence of shocks, below we compute the age and mechanical power of the bubble following previous works on shock-ionised bubbles (e.g. Pakull et al. 2010; Soria et al. 2021).

Interestingly, the inner parts of the nebula also show a clear indication of strong EUV/X-ray excitation. This is revealed by the high [O III] $\lambda$ 5007/H $\beta$   $> 5$  close to the source and south of it (Figure 11), surrounded by a region of weakly ionised gas (Figure 12), indicative of hard ionising radiation, in good agreement with the findings from Pakull & Mirioni (2002). This morphology, a cavity with an X-ray ionised nebula in its interior, is in many respects very similar to the bubble around IC 342 X-1 reported by Roberts et al. (2003). The morphology of the X-ray ionised region is also reminiscent of the prototypical photoionised nebula around Holmberg II X-1, which shows an area of high excitation close to the source (traced by the He II  $\lambda$ 4686 line), and strong [O I] $\lambda$ 6300 emission in the outer parts (Pakull & Mirioni 2002; Kaaret et al. 2004; Lehmann et al. 2005). We have also seen that some of these regions fall in the AGN-LINER classification locus according to the BPT diagrams (Figure 11). Similar classification was found by Berghea & Dudik (2012) using infrared observations of Holmberg II X-1 and NGC 6946 X-1, which are typical photoionised dominated nebulae (e.g. Abolmasov et al. 2006). EUV/X-ray excitation is also supported by the line ratios predicted by the MAPPINGS libraries, which cannot account for the combined high [O I] $\lambda$ 6300/H $\alpha$  or [O III] $\lambda$ 5007/H $\beta$  ratios, ruling out shocks as the main source of ionisation. Thus, NGC 1313 X-1 shows signs of ionising the surrounding medium by means of both shocks and EUV/X-ray radiation, which highlights the complex morphology of the nebula and enormous power of ULXs in ionising the ISM. This has been recently highlighted in the work of Simmonds et al. (2021),

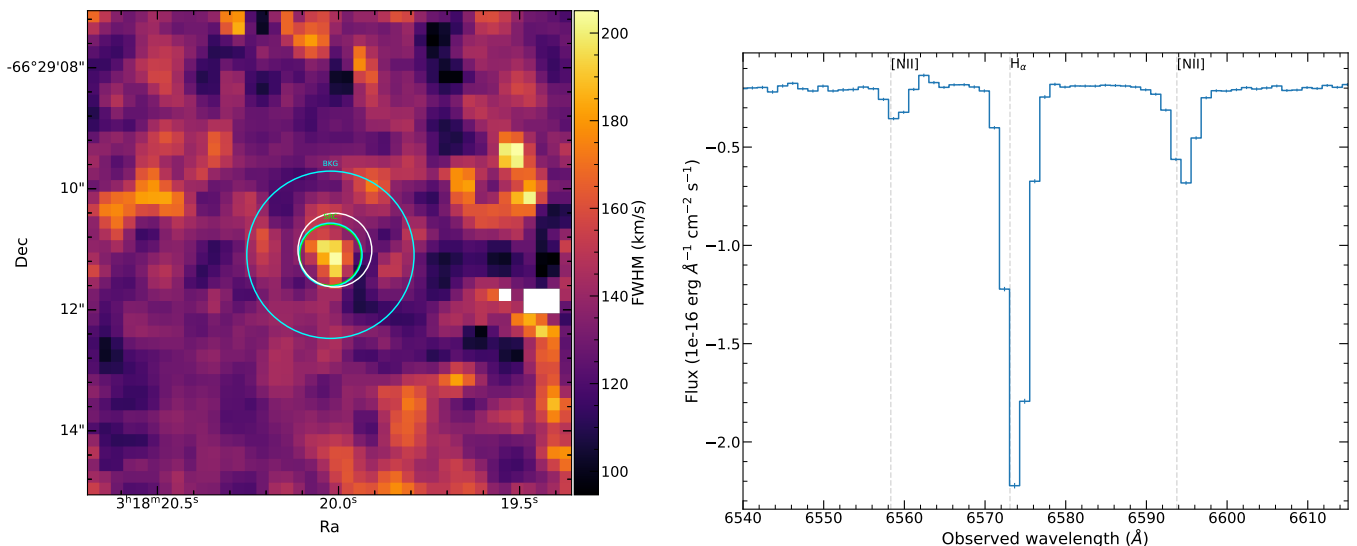


**Fig. 17.** Extraction regions and optical spectrum of the counterpart. (left) Dispersion map for the [O I]λ6300 line showing the enhancement around the ULX position and the extraction regions used. The extraction regions for the source and background are shown in green and cyan, respectively, whereas the white circle shows the ULX positions as determined in Section 2. (right) MUSE background-subtracted spectrum of the optical counterpart around the Hα-[N II] complex. The main nebular lines are labelled and their expected positions based on the redshift of the galaxy are indicated with grey dashed lines.

which have shown that a combination of realistic ULX broadband and stellar population spectra can reproduce the nebular He II λ4686 emission seen in low-metallicity galaxies, whose origin remains unclear.

Our study also suggest that ULX bubbles might be more complex than revealed by long-slit spectroscopy alone. In this regard, it is surprising that the nebula around NGC 5408 X-1 seems to show no signs of shock excitation (Cseh et al. 2012) and displays a much smaller bubble ( $\sim 60$  pc; Grisé et al. 2012), given the detection of winds in X-rays (Pinto et al. 2016) with similar outflow velocities ( $\sim 0.2c$ ). We note that Cseh et al. (2012) probed a small ( $2'' \times 1''$ ) region around NGC 5408 X-1 based on the [O III]λ5007 line map, whereas here we show that the [O III]λ5007 emission is concentrated close to the source in the high-excitation regions. In fact, a similar conclusion was reached by Mirioni (2002) after performing long-slit spectroscopy of the high-excitation region around NGC 1313 X-1, thereby missing the shock-excited regions at further distances from the source. We believe that a more thorough study using IFU spectroscopy is needed to completely rule out the presence of shocks in sources such as NGC 5408 X-1.

The  $452 \times 266$  pc bubble around NGC 1313 X-1 sits at the high end of the largest optical nebulae ever detected to date, comparable in size to the shocked bubble around the ULX in NGC 1313 X-2 (Pakull et al. 2005) or the bubble around Holmberg IX X-1 (Grisé et al. 2011). The detailed analysis of the nebula around NGC 5585 X-1 presented by Soria et al. (2021) allows us to compare the X-ray properties and bubble characteristics of these two sources. The bubble around NGC 5585 X-1 is also similar in size and morphology with respect to that of NGC 1313 X-1 and, as stated above, shows similar strong broadening towards the edges of the bubble with similar FWHM values and [S II]/Hα and [O I]λ6300/Hα ratios, typical of shock-dominated bubbles. However, it is interesting to observe that the bubble around NGC 5585 X-1 shows no signs of EUV/X-ray excitation, with [O III]λ5007/Hβ only reaching values of  $\sim 1.6$  ( $\log([O III]/H\beta) \sim 0.2$ ) well within the HII region classi-

fication in the [N II]/Hα diagram (cf. Figure 11). While NGC 1313 X-1 reaches unabsorbed luminosities of  $\sim 1.8 \times 10^{40}$  erg/s (Gúrpide et al. 2021a), NGC 5585 X-1 only reaches  $\sim 4 \times 10^{39}$  erg/s (Soria et al. 2021). The difference in ionising photons between these two sources may therefore account for the different [O III]λ5007/Hβ ratios. This may suggest that the dimmer luminosity of NGC 5585 X-1 is intrinsic and not due to a geometrical effect due to an unfavourable viewing angle in which the funnel axis could have been strongly misaligned with respect to our line of sight. Interestingly, NGC 1313 X-1 switches between soft and hard ultraluminous states (Sutton et al. 2013), thought to belong to the ULXs for the which the intense accretion rate leads to the formation of a supercritical disk-wind funnel (Shakura & Sunyaev 1973; Poutanen et al. 2007), whereas NGC 5585 X-1 belongs to the so-called broadened disk type (Soria et al. 2021), which are thought to be sources close or at the Eddington limit (e.g. Middleton et al. 2013). This may be consistent with the implied higher accretion rate in NGC 1313 X-1. Alternatively, the gas in the cavity created by NGC 5585 X-1 might more rarefied than that of NGC 1313 X-1. We show below that the mechanical power of NGC 1313 X-1 is comparable to that of NGC 5585 X-1. If the outflow rate depends on the Eddington accretion rate (e.g. Shakura & Sunyaev 1973; Poutanen et al. 2007), this may instead imply that the Eddington accretion rates of the two sources are similar, and that NGC 5585 X-1 might be viewed through an unfavourable viewing angle compared to NGC 1313 X-1. Another possibility, if indeed both sources have similar Eddington accretion rates, is that NGC 5585 X-1 hosts a lighter compact object, which could also account for its dimmer luminosity.

In this respect, it is unclear whether we can derive some conclusions from the morphology of the X-ray ionised nebula with regard to the level of anisotropy of the X-ray emission in NGC 1313 X-1. The offset between the peak of the [O III]λ5007/Hβ ratio and the ULX position might be expected (e.g. Halpern & Grindlay 1980), given the rather low ionisation potential to doubly ionise oxygen (35.1 eV). The fact that the X-ray ionised re-



gion is only seen south of the ULX is likely due to the nebula being density-bounded in the north direction, given the absence of significant H $\alpha$  emission there (Figure 5). Therefore, the nebula might not directly probe the degree of anisotropy of the X-ray emission. Observations in the [O IV] 25.89  $\mu$ m or the He II  $\lambda$ 4686 lines would be of interest as they should trace more closely the high-excitation regions closer to the ULX. The flux of the He II  $\lambda$ 4686 photon-counting line (e.g. Pakull & Angebault 1986) or photoionisation modelling of these regions might provide useful constraints on the EUV spectra of the source, degree of anisotropy, and/or inclination (e.g. Kaaret et al. 2004; Abolmasov et al. 2008, 2009; Berghea et al. 2010). MUSE observations of the nebulae around the Galactic supercritically accreting source SS433 (Dubner et al. 1998), long speculated to be an edge-on ULX (King 2002; Fabrika 2004; Middleton et al. 2021), and ULXs for which the inclination is suspected to be higher than for NGC 1313 X-1, such as NGC 5408 X-1 (Middleton et al. 2011), might also offer interesting comparisons with that of NGC 1313 X-1 to constrain the inclination of these systems and the relationship between the bubble morphology and the accretion flow geometry.

#### 4.1. Age and mechanical power of the ULX bubble

The characteristic age of the bubble can be estimated assuming that a spherically expanding bubble has been carved by a steady wind with mechanical power  $P_{\text{mec}}$  over the bubble lifetime ( $t$ ) (Weaver et al. 1977). The evolution of the bubble radius ( $R$ ) over time as a function of  $P_{\text{mec}}$  and the mass density of the unshocked ISM ( $\rho$ ) is given by

$$R = \left( \frac{125}{154\pi} \right)^{1/5} (P_{\text{mec}}/\rho)^{1/5} t^{3/5}. \quad (5)$$

We assume that the bubble expands into a neutral ISM, which has a mean molecular weight  $\mu = 1.38$ , and thus  $\rho = \mu m_p n_{\text{ISM}}$ , where  $m_p$  is the proton mass and  $n_{\text{ISM}}$  is the hydrogen number density estimated in Section 3.5. The expansion velocity is therefore

$$v_{\text{exp}} = \frac{dR}{dt} = \frac{3}{5} R/t, \quad (6)$$

which we take as  $v_{\text{shock}}$ . The age of the bubble is then  $t = \frac{3R}{5v_{\text{exp}}}$ . From these expressions the mechanical power can be estimated as

$$P_{\text{mec}} = \left( \frac{154\pi}{125} \right) R^2 v_{\text{shock}}^3 (\mu m_p n_{\text{ISM}}). \quad (7)$$

With these formulae we estimate the age and the mechanical power considering the major and minor semi-axes of the bubble for a typical  $v_{\text{shock}} = 170$  km/s. The results are given in Table 5. The estimated ages are found to be  $(4.6 \pm 0.7) \times 10^5$  yr and  $(7.8 \pm 1.2) \times 10^5$  yr for the minor and major axes, respectively, so a typical age would be  $\sim 6.2 \times 10^5$  yr. For the mechanical power, we find  $(1.9 \pm 1) \times 10^{40}$  erg/s and  $(5.5 \pm 3) \times 10^{40}$  erg/s, essentially consistent within the uncertainties for both semi-axes.

As stated in Section 3.5, the exact factor relating  $v_{\text{shock}}$  and FWHM is rather uncertain. Assuming the perhaps more conservative case in which  $v_{\text{shock}} = \text{FWHM}$ , which we take as  $\sim 110$  km/s, the average FWHM from all regions (Table 5), we find slightly greater mechanical power for the larger axis, but in good agreement within the uncertainties with the estimates given above. This is in part because the estimated  $n_{\text{ISM}}$  values

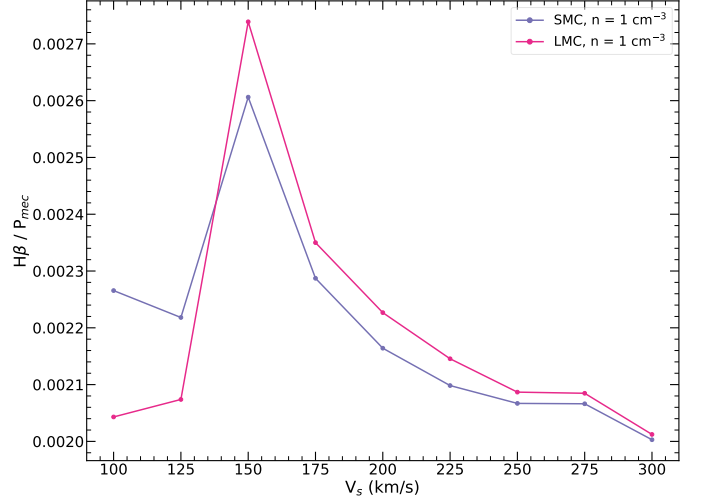


**Fig. 18.** Ratio of the H $\beta$  luminosity to the mechanical power as a function of  $v_{\text{shock}}$  for a plausible range of metallicities (SMC and LMC as derived in Section 3.4) assuming equipartition for the magnetic field value.

are higher for lower shock velocities (cf. Equation 3) and offset the lower shock velocity when estimating the mechanical power. We thus consider the estimates given above as a good figure for the mechanical power of the source. The age of the bubble would obviously increase by a factor of  $\sim 1.47$ , thus a reasonable range may be  $t \sim (6.2\text{--}8.7) \times 10^5$  yr.

Another method commonly used to estimate the mechanical power is to use some of the optical lines as a proxy (e.g. Pakull et al. 2010; Soria et al. 2014). To this end, we used the H $\beta$  line as it has a weak dependence on the shock velocity, whereas we have already determined the pre-shock gas density of the ISM (which we take as  $n_{\text{ISM}} = 1 \text{ cm}^{-3}$ ) and the metallicity around NGC 1313 X-1. From standard bubble theory (Weaver et al. 1977) we expect the total radiative luminosity of the shock to be  $L_T = 27/77 P_{\text{mec}}$ . The total radiative luminosity of the shock as a function of  $v_{\text{shock}}$  can be estimated from Equation 3.3 in Dopita & Sutherland (1996) (see also Soria et al. 2014),

$$L_T = \frac{1}{2} (\mu m_p n_{\text{ISM}}) v_s^3 = 1.14 \times 10^{-3} \left( \frac{v_s}{100 \text{ km s}^{-1}} \right)^3 n_{\text{ISM}} \text{ erg cm}^{-2} \text{ s}^{-1}, \quad (8)$$

where we have assumed  $\mu = 1.38$  as above. The total radiative luminosity of the H $\beta$  line as a function of  $v_{\text{shock}}$  can be obtained from the MAPPINGS libraries (Allen et al. 2008)<sup>9</sup>. We therefore calculated the fraction of power radiated in the H $\beta$  line as a function of  $v_{\text{shock}}$  for the best set of abundances derived in Section 3.4 (LMC and SMC). The resulting calculation is shown in Figure 18. We assume equipartition magnetic field values in the calculation, but the results are equivalent for ISM magnetic field values in the 1–10  $\mu$ G range. From the shock velocities derived in Table 5, we find  $L_{\text{H}\beta} \approx (2.3\text{--}2.6) \times 10^{-3} P_{\text{mec}}$ .

We now need to estimate the total luminosity in the H $\beta$  emitted by shocks in the bubble. For this we simply add the  $L_{\text{H}\beta}$  of each of the five shocked regions discussed in Figure 6 (Table 5) which gives  $\Sigma L_{\text{H}\beta} = (5.33 \pm 0.01) \times 10^{37}$  erg/s. We note that while there might be some contribution to the H $\beta$  luminosity

<sup>9</sup> Here we use the Allen et al. (2008) tables as those compiled by Alarie & Morisset (2019) do not include these values.

coming from EUV/X-ray excitation, notably for region 5, this is likely compensated by the fact that we might be missing some H $\beta$  flux around regions 3, 4, and 6 given the coarser regions employed (Figure 6). We thus consider these regions adequate in order to provide an order of magnitude estimate on  $P_{\text{mec}}$ . With these values we obtained  $P_{\text{mec}} \approx (3.8\text{--}4.3) \times 10^2 \Sigma L_{\text{H}\beta} \approx (2.2 \pm 0.3) \times 10^{40}$  erg/s. An approximate upper limit on the mechanical power using this method may be obtained by considering all the flux emitted in the whole bubble, approximated as the cyan ellipse in Figure 6, and subtracting the flux emitted due to EUV/X-ray excitation, which we approximate as the polygon classified as intermediate and AGN in the [N II]/H $\alpha$  BPT diagram (Figure 11) south of the ULX. We measure  $\Sigma L_{\text{H}\beta} = 1 \times 10^{38}$  erg/s, and therefore we estimate  $P_{\text{mec}} \lesssim 4.0\text{--}4.5 \times 10^{40}$  erg/s. If we additionally exclude the flux from region 5, which we saw is likely dominated by X-ray ionisation, we obtain  $P_{\text{mec}} \lesssim 3.5\text{--}4.0 \times 10^{40}$  erg/s.

We thus conclude that the estimated mechanical power is comparable to or higher than the X-ray luminosity of the source. This is in agreement with the estimates obtained from wind detections using X-ray spectroscopy (Pinto et al. 2016; Walton et al. 2016), which also revealed that the wind dominates the energy output of the source. We note that this agreement is remarkable given that these estimates are completely independent. The mechanical power of the NGC 1313 X-1 is comparable to that found for microquasars such as NGC 7793–S26 or M83 Q1 (Soria et al. 2014), which also display mechanical powers exceeding their radiative luminosities, whereas the estimated age is commensurate with other ULX bubbles such as the one around the ULX in NGC 5585 (Soria et al. 2021) or IC 342 X-1 (Cseh et al. 2012).

#### 4.2. Age and explosion energy of the supernova remnants

We first consider the case in which these SNRs are in the free-adiabatic expanding phase, where the expansion can be described by the well-known Sedov-Taylor self-similar solution. The radius of the SNR since the time of explosion ( $t$ ) is defined solely by the initial explosion energy  $E$  and the density of the ambient medium ( $\rho$ ),

$$R = \left( \frac{2.026E}{\rho} \right)^{1/5} = \left( \frac{2.026E}{\mu n_{\text{ISM}} m_p} \right)^{1/5} t^{2/5}, \quad (9)$$

for which we have assumed neutral hydrogen, as in the previous section. The expansion velocity is therefore

$$V = \frac{2R}{5t}. \quad (10)$$

Using our estimates from Section 3.4 for the shock velocity and our estimates for  $n_{\text{ISM}}$  from Section 5 for a radius of 17.5 pc, we estimate  $t_{\text{SNR1}} = (16 \pm 2) \times 10^4$  yr and  $t_{\text{SNR2}} = (17 \pm 2) \times 10^4$  yr. However, the energies obtained under this assumption are  $\sim 10^{49}$  erg, two orders of magnitude below the canonical value of  $10^{51}$  erg. Assuming a canonical energy of  $10^{51}$  erg and using the analytical expressions from Cioffi et al. (1988), we find that the radius at which the Sedov-Taylor expansion stage ends is  $\sim 19$  pc and  $\sim 17$  pc for SNR 1 and SNR 2, respectively. It is thus possible that these are evolved SNRs that have already entered the so-called pressure-driven snowplough phase, in which radiative losses become important (Cioffi et al. 1988). This might also be supported by the presence of several strong forbidden lines in their spectra (Figures 5 and 10).

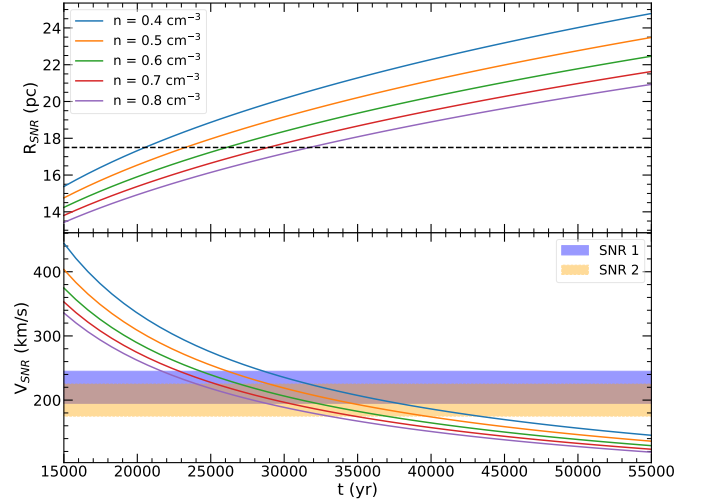


**Fig. 19.** Evolution of the radius and expansion velocity of a SNR (green shaded areas) as a function of time for the pressure-drive snowplough phase using the analytical expressions from Cioffi et al. (1988) for an initial explosion energy of  $0.5 \times 10^{51}$ . The evolution is calculated for the typical range of values found for  $n_{\text{ISM}}$  in Section 3.5 (Table 5). The dashed line indicates the radii of the SNRs measured from the HST images (Figure 9) and the blue and yellow shaded areas represent the range of shock velocities determined in Section 3.4 (Table 5) for SNR 1 and 2, respectively.

We therefore refine our calculation by using the analytical expressions from (Cioffi et al. 1988, see also Fesen et al. 2020b). Figure 19 shows the evolution of the radius and the SNR expansion velocity as a function of time. We find good agreement with the calculations for the radii and for the velocities assuming an initial explosion energy of  $0.5 \times 10^{51}$  erg. From the figure we can estimate  $t_{\text{SNR1}} = 2.4\text{--}2.7 \times 10^4$  yr and  $t_{\text{SNR2}} = 2.5\text{--}3.4 \times 10^4$  yr (for a fixed  $E = 0.5 \times 10^{51}$  erg). We find  $0.3 < E < 0.8 \times 10^{51}$  erg as a plausible range of energies to match the observed radii and derived velocities.

We can do a similar exercise for the ULX bubble, assuming again that, given its large size ( $R > 130$  pc; Table 5), it is an evolved remnant in the snowplough phase. The expression for the energy explosion in the radiative phase is (Cioffi et al. 1988)

$$E_{51} = 6.8 \times 10^{43} \left( \frac{R}{\text{pc}} \right)^{3.16} \left( \frac{v_{\text{exp}}}{\text{kms}^{-1}} \right)^{1.35} \left( \frac{n_{\text{ISM}}}{\text{cm}^{-3}} \right)^{1.16} \text{ erg}, \quad (11)$$

where following Cseh et al. (2012) we also adopted the metallicity factor  $\xi_m$  as unity for simplicity. Taking the values from Table 5 we arrive at  $E = 188\text{--}990 \times 10^{51}$  erg for the minor and major axes, respectively, more than two orders of magnitude above the typical SNR explosion energy and in the range of estimates of other ULX bubbles (e.g. Pakull & Mirioni 2002; Berghea et al. 2020). This is perhaps not surprising as SNRs are not expected to remain optically bright once expanded beyond  $\sim 100$  pc for an input canonical energy of  $10^{51}$  erg (Braun et al. 1989), and indeed the largest and oldest known SNRs have radii of just  $\approx 50$  pc (see e.g. Leahy et al. 1986; Williams et al. 2004; Fesen et al. 2020a, and references therein). Therefore these results are in good agreement with previous works (e.g. Pakull & Mirioni 2002; Cseh et al. 2012; Urquhart et al. 2019; Berghea et al. 2020) which suggest instead that a continuous injection of energy is more likely to explain the cavities found around some ULXs. However, we note that we cannot exclude the possibility that the ULX perturbed the SNR that gave birth to the compact

object. This would be similar to the case of the SS433/W50 nebula (Goodall et al. 2011, although see also Ohmura et al. 2021) or its potentially younger version Circinus X-1 (Heinz et al. 2015; Coriat et al. 2019).

## 5. Conclusions

We have shown that NGC 1313 X-1 ionises a region of  $452 \times 266$  pc via EUV/X-ray–X-ray excitation and shocks. Thanks to the simultaneous spectro-imaging capabilities of MUSE, we were able to diagnose the main sources of ionisation of the bubble in a spatially resolved manner: the inner regions close to the ULX show all the hallmarks of an X-ray ionised region, whereas the outer edges shows clear signs of shock-excitation. The latter is revealed by the strong broadening of the nebular lines at the edges of the bubble combined with the high line-of-sight velocity measured inside the bubble cavity close to the source, strongly suggesting that the bubble is being inflated by a wind. The elongated shape of the nebula may point to the presence of jet activity, and thus radio observations would be of great interest here. Future observations probing high-excitation lines of the X-ray ionised nebula inside the bubble might be of interest to constrain the degree of beaming of the source.

The mechanical power is found to be in excess of  $10^{40}$  erg/s, suggesting that the mechanical power of the source is comparable or even higher than the radiative throughput. This is in line with other estimates made by Pakull et al. (2010), Soria et al. (2014) and Soria et al. (2021), suggesting that the mechanical feedback in the super-Eddington regime is superior to the radiative one. Obtaining a statistical sample of ULXs with estimated mechanical and radiative powers will be of interest to constrain the energy that goes into powering the wind, its dependency with the mass-accretion rate, and its link with the class of less-luminous microquasars with equally strong super-Eddington mechanical powers, such as SS433 or NGC 300 S10 (Urquhart et al. 2019; McLeod et al. 2019). The high mechanical power of ULXs make them good sources for cosmic-ray acceleration (Inoue et al. 2017; Abeysekara et al. 2018), which could be targeted in the future with the Cherenkov Telescope Array (Consortium 2011), the next-generation of ground-based gamma-ray observatories.

With this work we hope to have highlighted the promising avenue that IFU spectroscopy provides in our understanding of the ULX bubble nebulae and the energetic feedback of the super-Eddington regime.

**Acknowledgements.** The authors are deeply grateful to M. Pakull and R. Soria for their careful read and constructive comments on an earlier version of this manuscript. We would also like to thank M. Coriat for his helpful comments on the discussion related to the presence of any jet-like signature. We finally thank I. Pastor-Marazuela for her comments which lead us to investigate and discover the two SNRs. This work has made use of data obtained from the Chandra Data Archive as well as observations made with the NASA/ESA Hubble Space Telescope and obtained from the Hubble Legacy Archive, which is a collaboration between the Space Telescope Science Institute (STScI/NASA), the Space Telescope European Coordinating Facility (ST-ECF/ESA), and the Canadian Astronomy Data Centre (CADCA/NRC/CSA). Software used: Python v3.8, mpdaf (Piqueras et al. 2017).

## References

Abeysekara, A. U., Albert, A., Alfaro, R., et al. 2018, *Nature*, 562, 82, bandiera\_abtest: a Cg\_type: Nature Research Journals Number: 7725 Primary\_atype: Research Publisher: Nature Publishing Group Subject\_term: High-energy astrophysics;Particle astrophysics Subject\_term\_id: high-energy-astrophysics;particle-astrophysics

Abolmasov, P., Fabrika, S., Sholukhova, O., & Afanasiev, V. 2007, *Astrophys. Bull.*, 62, 36

Abolmasov, P., Fabrika, S., Sholukhova, O., & Kotani, T. 2008, arXiv:0809.0409 [astro-ph], arXiv: 0809.0409 version: 1

Abolmasov, P., Karpov, S., & Kotani, T. 2009, *Publications of the Astronomical Society of Japan*, 61, 213

Abolmasov, P. K., Fabrika, S. N., & Sholukhova, O. N. 2006, *Proceedings of the International Astronomical Union*, 2, 229, publisher: Cambridge University Press

Alarie, A. & Morisset, C. 2019, *Revista Mexicana de Astronomia y Astrofisica*, 55, 377

Allen, M. G., Groves, B. A., Dopita, M. A., Sutherland, R. S., & Kewley, L. J. 2008, *The Astrophysical Journal Supplement Series*, 178, 20

Bachetti, M., Harrison, F. A., Walton, D. J., et al. 2014, *Nature*, 514, 202

Bachetti, M., Rana, V., Walton, D. J., et al. 2013, *ApJ*, 778, 163

Bacon, R., Conseil, S., Mary, D., et al. 2017, *A&A*, 608, A1

Baldwin, J. A., Phillips, M. M., & Terlevich, R. 1981, *Publications of the Astronomical Society of the Pacific*, 93, 5

Berghea, C. T. & Dudik, R. P. 2012, *ApJ*, 751, 104, publisher: IOP Publishing

Berghea, C. T., Dudik, R. P., Weaver, K. A., & Kallman, T. R. 2010, *The Astrophysical Journal*, 708, 364

Berghea, C. T., Johnson, M. C., Secrest, N. J., et al. 2020, *ApJ*, 896, 117, publisher: American Astronomical Society

Braun, R., Goss, W. M., & Lyne, A. G. 1989, *The Astrophysical Journal*, 340, 355, aDS Bibcode: 1989ApJ...340..355B

Calzetti, D., Armus, L., Bohlin, R. C., et al. 2000, *ApJ*, 533, 682, publisher: American Astronomical Society

Carpano, S., Haberl, F., Maitra, C., & Vasilopoulos, G. 2018, *Monthly Notices of the Royal Astronomical Society: Letters*, 476, L45

Cioffi, D. F., McKee, C. F., & Bertschinger, E. 1988, *The Astrophysical Journal*, 334, 252, aDS Bibcode: 1988ApJ...334..252C

Consortium, T. C. 2011, *Exp Astron*, 32, 193, arXiv: 1008.3703

Coriat, M., Fender, R. P., Tasse, C., et al. 2019, *Monthly Notices of the Royal Astronomical Society*, 484, 1672

Cseh, D., Corbel, S., Kaaret, P., et al. 2012, *ApJ*, 749, 17

Dewey, D. 2010, *Space Science Reviews*, Volume 157, Issue 1-4, pp. 229-248, 157, 229

Dopita, M. A., Payne, J. L., Filipović, M. D., & Pannuti, T. G. 2012, *Monthly Notices of the Royal Astronomical Society*, 427, 956, aDS Bibcode: 2012MNRAS.427..956D

Dopita, M. A. & Sutherland, R. S. 1996, *The Astrophysical Journal Supplement Series*, 102, 161

Dors, O. L., Hägle, G. F., Cardaci, M. V., & Krabbe, A. C. 2017, *Monthly Notices of the Royal Astronomical Society*, 466, 726, aDS Bibcode: 2017MNRAS.466..726D

Dubner, G. M., Holdaway, M., Goss, W. M., & Mirabel, I. F. 1998, *AJ*, 116, 1842, publisher: American Astronomical Society

Egorov, O. V., Lozinskaya, T. A., & Moiseev, A. V. 2017, *Mon Not R Astron Soc Lett*, 467, L1, publisher: Oxford Academic

Epinat, B., Tasca, L., Amram, P., et al. 2012, *Astronomy and Astrophysics*, 539, A92

Fabrika, S. 2004, *Astrophysics and Space Physics Reviews*, 12, 1

Fabrika, S. N., Atapin, K. E., Vinokurov, A. S., & Sholukhova, O. N. 2021, *Astrophys. Bull.*, 76, 6, arXiv: 2105.10537

Feng, H. & Kaaret, P. 2006, *ApJ*, 650, L75

Fesen, R. A. & Hurford, A. P. 1996, *The Astrophysical Journal Supplement Series*, 106, 563, aDS Bibcode: 1996ApJS...106..563F

Fesen, R. A., Weil, K. E., Raymond, J. C., et al. 2020a, *Monthly Notices of the Royal Astronomical Society*, 498, 5194, aDS Bibcode: 2020MNRAS.498.5194F

Fesen, R. A., Weil, K. E., Raymond, J. C., et al. 2020b, *Monthly Notices of the Royal Astronomical Society*, 498, 5194

Fürst, F., Walton, D., Harrison, F., et al. 2016, *The Astrophysical Journal*, 831

Gaia Collaboration, A. G. A. Brown, Vallenari, A., et al. 2018, *A&A*, 616, A1, publisher: EDP Sciences

Gladstone, J. C., Roberts, T. P., & Done, C. 2009, *Mon Not R Astron Soc*, 397, 1836

Goodall, P. T., Alouani-Bibi, F., & Blundell, K. M. 2011, *Monthly Notices of the Royal Astronomical Society*, 414, 2838

Grisé, F., Kaaret, P., Corbel, S., et al. 2012, *ApJ*, 745, 123

Grisé, F., Kaaret, P., Pakull, M. W., & Motch, C. 2011, *The Astrophysical Journal*, 734, 23

Gutkin, J., Charlot, S., & Bruzual, G. 2016, *Monthly Notices of the Royal Astronomical Society*, 462, 1757

Gúrpide, A., Godet, O., Koliopanos, F., Webb, N., & Olive, J.-F. 2021a, *A&A*, 649, A104, publisher: EDP Sciences

Gúrpide, A., Godet, O., Vasilopoulos, G., Webb, N. A., & Olive, J.-F. 2021b, *A&A*, 654, A10



- Halpern, J. P. & Grindlay, J. E. 1980, *The Astrophysical Journal*, 242, 1041, aDS Bibcode: 1980ApJ...242.1041H
- Heinz, S., Burton, M., Braiding, C., et al. 2015, *ApJ*, 806, 265, publisher: American Astronomical Society
- Inoue, Y., Lee, S.-H., Tanaka, Y. T., & Kobayashi, S. B. 2017, *Astroparticle Physics*, 90, 14, aDS Bibcode: 2017APh....90...14I
- Israel, G. L., Belfiore, A., Stella, L., et al. 2017, *Science*, 355, 817
- Jiang, Y.-F., Stone, J. M., & Davis, S. W. 2014, *ApJ*, 796, 106
- Kaaret, P., Feng, H., Wong, D. S., & Tao, L. 2010, *ApJL*, 714, L167
- Kaaret, P., Ward, M. J., & Zezas, A. 2004, *Mon Not R Astron Soc*, 351, L83
- Kauffmann, G., Heckman, T. M., Tremonti, C., et al. 2003, *Monthly Notices of the Royal Astronomical Society*, 346, 1055
- Kewley, L. J., Dopita, M. A., Leitherer, C., et al. 2013, *The Astrophysical Journal*, 774, 100
- Kewley, L. J., Dopita, M. A., Sutherland, R. S., Heisler, C. A., & Trevena, J. 2001, *The Astrophysical Journal*, 556, 121
- Kewley, L. J., Groves, B., Kauffmann, G., & Heckman, T. 2006, *Monthly Notices of the Royal Astronomical Society*, 372, 961
- King, A. 2002, *Monthly Notices of the Royal Astronomical Society*, 335
- King, A. R., Davies, M. B., Ward, M. J., Fabbiano, G., & Elvis, M. 2001, *ApJ*, 552, L109
- Koliopanos, F., Vasilopoulos, G., Godet, O., et al. 2017, *A&A*, 608, A47
- Kopsacheili, M., Zezas, A., Leonidaki, I., & Boumip, P. 2021, *Monthly Notices of the Royal Astronomical Society*, 507, 6020
- Kuncarayakti, H., Maeda, K., Anderson, J. P., et al. 2016, *Monthly Notices of the Royal Astronomical Society*, 458, 2063
- Lara-López, M. A., Zinchenko, I. A., Pilyugin, L. S., et al. 2021, *The Astrophysical Journal*, 906, 42
- Law, D. R., Ji, X., Belfiore, F., et al. 2021, arXiv:2011.06012 [astro-ph], arXiv: 2011.06012
- Leahy, D. A., Naranan, S., & Singh, K. P. 1986, *Monthly Notices of the Royal Astronomical Society*, 220, 501
- Lehmann, I., Becker, T., Fabrika, S., et al. 2005, *A&A*, 431, 847, number: 3 Publisher: EDP Sciences
- Liu, J.-F., Bai, Y., Wang, S., et al. 2015, *Nature*, 528, 108, number: 7580 Publisher: Nature Publishing Group
- Matonick, D. M. & Fesen, R. A. 1997, *The Astrophysical Journal Supplement Series*, 112, 49, aDS Bibcode: 1997ApJS...112...49M
- McLeod, A. F., Scaringi, S., Soria, R., et al. 2019, *Monthly Notices of the Royal Astronomical Society*, 485, 3476, arXiv: 1903.00005
- Middleton, M. J., Heil, L., Pintore, F., Walton, D. J., & Roberts, T. P. 2015, *Monthly Notices of the Royal Astronomical Society*, 447, 3243
- Middleton, M. J., Miller-Jones, J. C. A., Markoff, S., et al. 2013, *Nature*, 493, 187
- Middleton, M. J., Roberts, T. P., Done, C., & Jackson, F. E. 2011, *Mon Not R Astron Soc*, 411, 644, publisher: Oxford Academic
- Middleton, M. J., Walton, D. J., Alston, W., et al. 2021, arXiv:1810.10518 [astro-ph], arXiv: 1810.10518
- Mineo, S., Gilfanov, M., & Sunyaev, R. 2012, *Monthly Notices of the Royal Astronomical Society*, 419, 2095
- Mirioni, L. 2002, PhD thesis, Univ. Strasbourg
- Momcheva, I. G., Lee, J. C., Ly, C., et al. 2013, *The Astronomical Journal*, 145, 47, aDS Bibcode: 2013AJ....145...47M
- Mushtukov, A. A., Portegies Zwart, S., Tsygankov, S. S., Nagirner, D. I., & Poutanen, J. 2021, *Monthly Notices of the Royal Astronomical Society*, 501, 2424
- Narayan, R., Sadowski, A., & Soria, R. 2017, *Mon Not R Astron Soc*, 469, 2997, publisher: Oxford Academic
- Ohmura, T., Ono, K., Sakemi, H., et al. 2021, *The Astrophysical Journal*, 910, 149
- Osterbrock, D. E. & Ferland, G. J. 2006, *Astrophysics of gaseous nebulae and active galactic nuclei*, 2nd. ed. by D.E. Osterbrock and G.J. Ferland. Sausalito, CA: University Science Books, 2006
- Pakull, M. W. & Angebault, L. P. 1986, *Nature*, 322, 511
- Pakull, M. W., Grise, F., & Motch, C. 2005, *Proc. IAU*, 1, 293, arXiv: astro-ph/0603771
- Pakull, M. W. & Grisé, F. 2008, 1010, 303, conference Name: A Population Explosion: The Nature & Evolution of X-ray Binaries in Diverse Environments Place: eprint: arXiv:0803.4345
- Pakull, M. W. & Mirioni, L. 2002, arXiv:astro-ph/0202488, arXiv: astro-ph/0202488
- Pakull, M. W., Soria, R., & Motch, C. 2010, *Nature*, 466, 209
- Peimbert, M., Sarmiento, A., & Fierro, J. 1991, *Publications of the Astronomical Society of the Pacific*, 103, 815, aDS Bibcode: 1991PASP.103..815P
- Pilyugin, L. S. & Grebel, E. K. 2016, *Monthly Notices of the Royal Astronomical Society*, 457, 3678
- Pinto, C., Mehdipour, M., Walton, D. J., et al. 2020a, *Mon Not R Astron Soc*, 491, 5702, publisher: Oxford Academic
- Pinto, C., Middleton, M. J., & Fabian, A. C. 2016, *Nature*, 533, 64
- Pinto, C., Soria, R., Walton, D. J., et al. 2021, *Monthly Notices of the Royal Astronomical Society*, 505, 5058, aDS Bibcode: 2021MNRAS.505.5058P
- Pinto, C., Walton, D. J., Kara, E., et al. 2020b, *Mon Not R Astron Soc*, 492, 4646, publisher: Oxford Academic
- Piqueras, L., Conseil, S., Shepherd, M., et al. 2017, arXiv:1710.03554 [astro-ph], arXiv: 1710.03554
- Poutanen, J., Lipunova, G., Fabrika, S., Butkevich, A. G., & Abolmasov, P. 2007, *Monthly Notices of the Royal Astronomical Society*, 377, 1187
- Pérez-Montero, E. 2017, *PASP*, 129, 043001, publisher: IOP Publishing
- Quintin, E., Webb, N., Gúrpide, A., Bachetti, M., & Fürst, F. 2021, arXiv:2103.11650 [astro-ph], arXiv: 2103.11650
- Ramsey, C. J., Williams, R. M., Gruendl, R. A., et al. 2006, *ApJ*, 641, 241
- Roberts, T. P., Goad, M. R., Ward, M. J., & Warwick, R. S. 2003, *Monthly Notices of the Royal Astronomical Society*, 342, 709, aDS Bibcode: 2003MNRAS.342..709R
- Rodríguez-Castillo, G. A., Israel, G. L., Belfiore, A., et al. 2020, *ApJ*, 895, 60, publisher: American Astronomical Society
- Russell, S. C. & Dopita, M. A. 1992, *The Astrophysical Journal*, 384, 508
- Ryder, S. D., Staveley-Smith, L., Malin, D., & Walsh, W. 1995, *The Astronomical Journal*, 109, 1592
- Ryon, J. E., Gallagher, J. S., Smith, L. J., et al. 2017, *The Astrophysical Journal*, 841, 92
- Sathyaprakash, R., Roberts, T. P., Walton, D. J., et al. 2019, *Monthly Notices of the Royal Astronomical Society*, 488, L35
- Shakura, N. I. & Sunyaev, R. A. 1973, *Astronomy and Astrophysics*, 24, 337
- Simmonds, C., Schaerer, D., & Verhamme, A. 2021, *Astronomy and Astrophysics*, 656, A127
- Soria, R., Long, K. S., Blair, W. P., et al. 2014, *Science*, 343, 1330
- Soria, R., Pakull, M. W., Motch, C., et al. 2021, *Monthly Notices of the Royal Astronomical Society*, 501, 1644
- Soto, K. T., Lilly, S. J., Bacon, R., Richard, J., & Conseil, S. 2016, *Monthly Notices of the Royal Astronomical Society*, 458, 3210, arXiv: 1602.08037
- Sutherland, R., Dopita, M., Binette, L., & Groves, B. 2018, *Astrophysics Source Code Library*, ascl:1807.005, aDS Bibcode: 2018ascl.soft07005S
- Sutton, A. D., Roberts, T. P., & Middleton, M. J. 2013, *Monthly Notices of the Royal Astronomical Society*, 435, 1758
- Takeuchi, S., Ohsuga, K., & Mineshige, S. 2013, *Publ Astron Soc Jpn Nihon Tenmon Gakkai*, 65, publisher: Oxford Academic
- Tully, R. B., Courtois, H. M., & Sorce, J. G. 2016, *AJ*, 152, 50
- Urquhart, R., Soria, R., Johnston, H. M., et al. 2018, *Monthly Notices of the Royal Astronomical Society*, 475, 3561
- Urquhart, R., Soria, R., Pakull, M. W., et al. 2019, *Monthly Notices of the Royal Astronomical Society*, 482, 2389
- Veilleux, S. & Osterbrock, D. E. 1987, *The Astrophysical Journal Supplement Series*, 63, 295
- Waisberg, I., Dexter, J., Olivier-Petrucci, P., Dubus, G., & Perraut, K. 2019, *Astronomy and Astrophysics*, 624, A127
- Walsh, J. R. & Roy, J.-R. 1997, *Monthly Notices of the Royal Astronomical Society*, 288, 726
- Walton, D. J., Fürst, F., Heida, M., et al. 2018, *ApJ*, 856, 128
- Walton, D. J., Middleton, M. J., Pinto, C., et al. 2016, *ApJL*, 826, L26
- Walton, D. J., Pinto, C., Nowak, M., et al. 2020, *Monthly Notices of the Royal Astronomical Society*, 494, 6012
- Weaver, R., McCray, R., Castor, J., Shapiro, P., & Moore, R. 1977, *The Astrophysical Journal*, 218, 377
- Weilbacher, P. M., Palsa, R., Streicher, O., et al. 2020, *A&A*, 641, A28, arXiv: 2006.08638
- Williams, R. M., Chu, Y.-H., Dickel, J. R., et al. 2004, *ApJ*, 613, 948, publisher: IOP Publishing
- Yang, L., Feng, H., & Kaaret, P. 2011, *ApJ*, 733, 118, publisher: American Astronomical Society

## Appendix A: Line ratios of the shocked regions

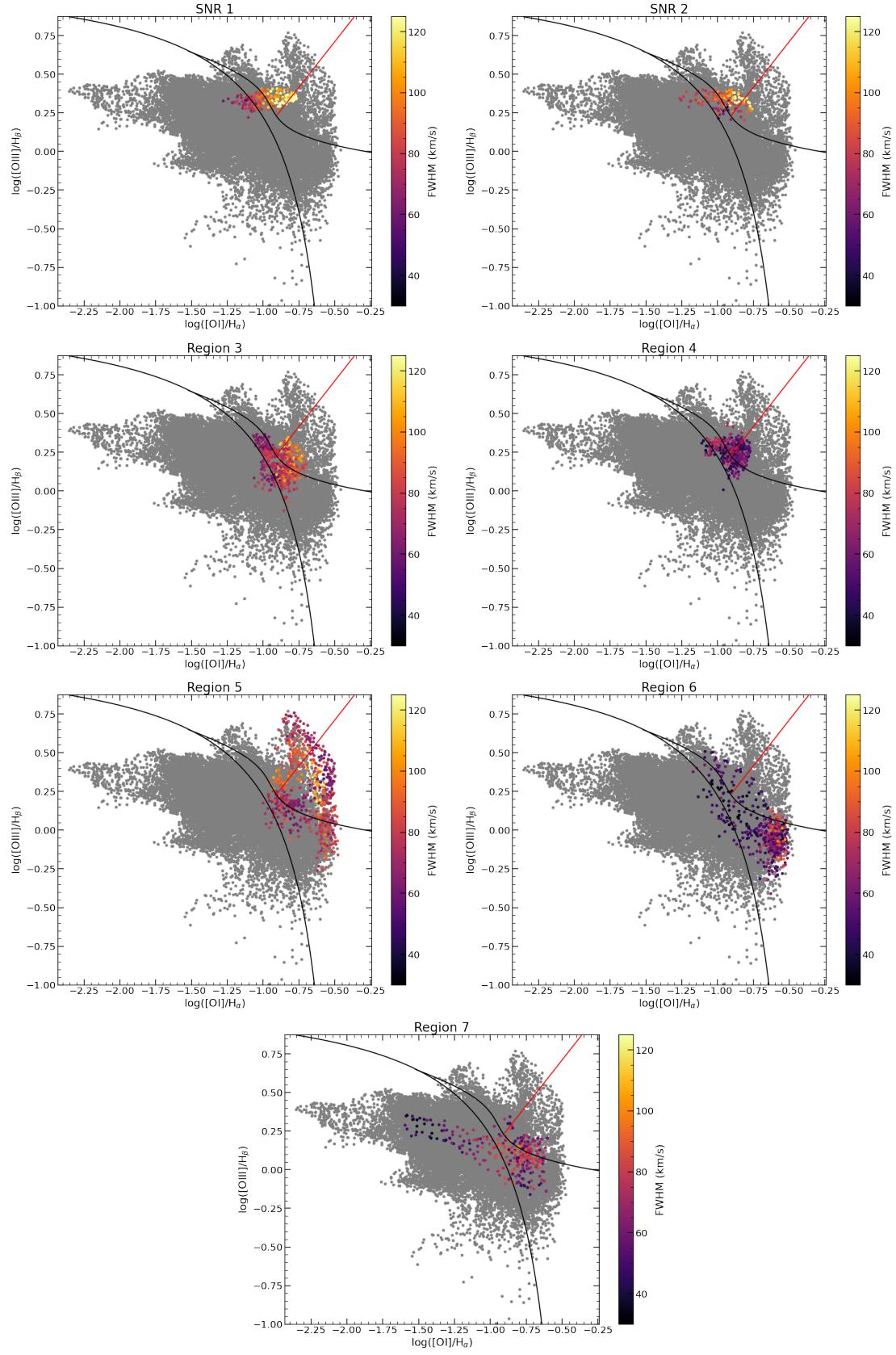


**Fig. A.1.** As in Figure 13, but showing only the different regions from Figure 6.